Research Internship
Academic Year 2024-2025

Particle separation in microfluidic channels by temperature variation

Théo Vidal <theo.vidal@ensta.fr>

Laboratorio de fluidodinámica
Facultad de Ingeniería – FIUBA

Av. Paseo Colón 850, C1063 Cdad. Autónoma de Buenos Aires

May 26, 2025 – August 22, 2025

ENSTA Academic Tutor: Romain Monchaux
<romain.monchaux@ensta.fr>
FIUBA Academic Tutor: Guillermo Osvaldo Artana <gartana@fi.uba.ar>

Acknowledgements

First of all, I would like to express my deepest gratitude to Dr Guillermo Osvaldo Artana, my internship supervisor, for welcoming me into his laboratory. This experience was particularly enriching, both in terms of new physics knowledge and practical research skills. I am also grateful to him for giving me the opportunity to travel to South America at a time when so many other laboratories had declined my application or had not responded. I come away from this internship deeply enriched culturally and linguistically.

I would also like to warmly thank the PhD students and researchers with whom I had the opportunity to collaborate. I would like to give a special mention to Tomás Robledo, who generously devoted his precious time to helping me set up my experimental procedures. I would like to extend a warm welcome to Franco, with whom I had excellent scientific discussions and who is working on a subject similar to mine, as well as the six French interns who were also present during this period.

Finally, I would like to thank my supervisor, Romain Monchaux, for kindly putting me in touch with Dr Artana and agreeing to supervise my internship. I would also like to thank Luc Pastur for his valuable advice on everyday life in Buenos Aires, which helped me approach this period with greater peace of mind.

Résumé

La microfluidique est un domaine de la mécanique des fluides qui étudie des écoulements dans des systèmes de dimension micrométrique ou inférieure. Les dispositifs sur puce (*Lab-on-a-chip*) sont étudiés au laboratoire afin de de caractériser le remplissage de microcanaux. Ce rapport de stage explore l'influence de la température sur ce remplissage capillaire, en combinant des expériences sur puces thermalisées par cellules Peltier, et des simulations numériques basées sur l'équation d'équilibre des pressions. Les résultats montrent une accélération de la dynamique avec la température due à la diminution de viscosité, avec des effets Marangoni observés sous gradients. Ces travaux proposent ainsi des axes d'étude et des modèles préliminaires, constituant une base pour de futurs développements au sein du laboratoire.

Mots-clés

Microfluidique, Laboratoire sur puce, Tension de surface, Thermocapillarité, Effet Marangoni

Abstract

Microfluidics is a field of fluid mechanics that studies flows in systems of micrometric or smaller dimensions. Lab-on-a-chip devices are investigated in the laboratory in order to characterise the filling of microchannels. This internship report explores the influence of temperature on this capillary filling, combining experiments on chips thermally controlled by Peltier cells, with numerical simulations based on the pressure balance equation. Results show an acceleration of the dynamics with increasing temperature, due to the decrease in viscosity, with Marangoni effects observed under gradients. This work thus proposes lines of research and preliminary models, forming a basis for future developments within the laboratory.

Keywords

Microfluidics, Lab-on-a-chip, Surface tension, Thermocapillarity, Marangoni effect

Table of contents

List of Figures

Introduction

My research internship took place from May 26 to August 22 of 2025 at the fluid mechanics laboratory (LFD, Laboratorio de fluidodinámica) of the Faculty of Engineering at the University of Buenos Aires, Argentina. This laboratory is headed by my supervisor, Dr. Guillermo Osvaldo Artana, and consists of about ten professors and doctoral students. I was also joined by six other French interns, thanks to the links between the LFD and numerous entities in France. The field of research is microfluidics, and the methods are based on the work of Pedro Manuel Garcia Eijo, who defended his thesis in August 2023.

The initial objective was to carry out exploratory work on the influence of temperature in microfluidics, starting by reproducing the experiments commonly performed in the laboratory. The ultimate goal was to perform local control, for example with electrical wires, but this could not be done due to setbacks and complexities.

As this work was exploratory in nature, I was able to approach it from several angles and develop this report, a summary that serves as a starting point for potential future work within the laboratory. This internship also aims to train me in research, particularly through an experimental approach that is very hands-on and new to me. Furthermore, I was not expected to obtain publishable results, as the LFD's internship programme is more focused on training and immersion in foreign culture, in Argentina, rather than on performing tasks and completing existing work.

First, we will cover the concepts of microfluidics that are essential to understanding the subject and carrying out physical experiments. Next, we will study my initial results concerning comb- and T-shaped microfluidic devices, as well as numerical simulations, laying the foundations for future studies on temperature. Thirdly, we will analyse a simpler system of straight channels at uniform temperature, following a change of strategy during the internship. Fourthly and finally, we will address the same channel but in the presence of temperature gradients, to suggest paths and start a consideration on the additional effects generated. A schedule for the internship is available on the first page of the appendix.

1 Job description

1.1 Surface tension, Laplace pressure and Marangoni effect

Within a fluid, the cohesive forces exerted on a molecule by its neighbours balance each other out, whereas at the interface with another medium, this cohesion is broken on one side, as illustrated in Figure 1. The **surface tension** σ is defined as the elementary work δW required to cause a variation $\mathrm{d}A$ in surface area:

$$\delta W = \sigma \ \mathrm{d}A \tag{1}$$

σ is expressed in $\mathrm{N/m}$ and depends on multiple physical and chemical properties: for water, it decreases with temperature [5] and with the concentration of certain substances, such as alcohol or soap - *surfactants*. The Bond number $\mathrm{Bo} = \frac{\rho g L^2}{\sigma}$ compares the volumetric and surface effects: a microfluidics study therefore always falls within the $\mathrm{Bo} < 1$ range. This internal cohesion manifests itself as a constraint $\oint_\Sigma \sigma \vec{s} \ \mathrm{d}l$, which, once injected into the forces balance equation, leads to two contributions in the stress tensor. On the one hand, a normal component called **Laplace pressure**:

$$\Delta P = P_{\mathrm{in}} - P_{\mathrm{out}} = \sigma \vec{\nabla} \cdot \vec{n} \tag{2}$$

with $\vec{\nabla} \cdot \vec{n}$ the curvature. On the other hand, a tangential constraint manifests in the presence of surface tension gradients, which is called the **Marangoni effect**:

$$\vec{f}_M = \vec{\nabla} \sigma \tag{3}$$

This phenomenon can be observed, for example, in a glass of wine: the fluid rises up the side of the glass as the alcohol evaporates, until the column of fluid becomes too heavy and gravity takes over again, forming “wine tears”.

1.2 Contact angle

In a three-phase system comprising a liquid in contact with a solid, all immersed in any fluid (in most cases, a gas) as illustrated in Figure 2, the liquid drop forms an angle with the solid surface called the **contact angle**. At equilibrium on a smooth surface, it is expressed by Young’s equation:

$$\sigma_{\mathrm{lf}} \cos \theta_{\mathrm{e}} = \sigma_{\mathrm{sf}} - \sigma_{\mathrm{sl}} \tag{4}$$

where σ_{lf}, σ_{sf} and σ_{sl} denote the surface tensions at the liquid-fluid, solid-fluid and solid-liquid interfaces, respectively. The wall is said to be hydrophilic for $\theta < 90°$ and hydrophobic for $\theta > 90°$. This contact angle can be observed in several ways, for instance by placing a drop of fluid on a surface using the method developed in Section 1.6.2 and shown on Figure 2 or by using a vertical

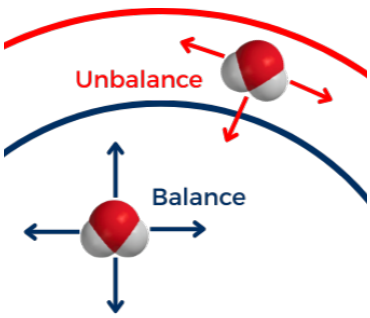

Figure 1: Cohesive forces acting on molecules inside (blue) and on the surface (red) of a fluid; the unbalance on the surface generates surface tension.

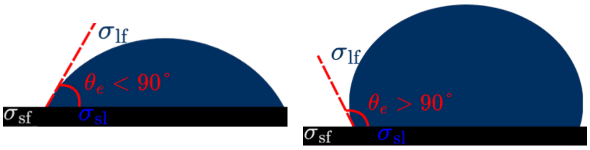

(a) Hydrophilic case

(b) Hydrophobic case

Figure 2: Diagram of the three-phase system forming a contact angle.

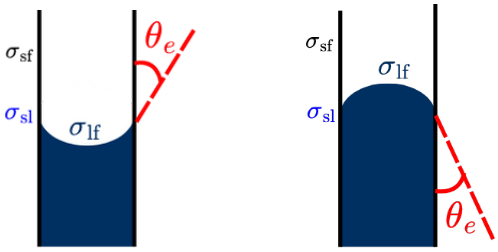

(a) Hydrophilic case (*Rise*)

(b) Hydrophobic case (*Recession*)

Figure 3: Capillary action on a fluid in a vertical microchannel.

column of fluid and observing the shape of the meniscus, as shown in Figure 3 - the result of the balance between surface tension and gravity. In the case of a rough surface, the apparent contact angle is generally smaller, and is given analytically in [6] by formula $\cos\theta_{\text{eff}} = r_s \cos\theta_e$, where r_s is the roughness coefficient, equal to 1 for a perfectly smooth surface and greater than 1 otherwise.

Out of equilibrium, the fluid forms a contact angle that may be different, the dynamic contact angle θ_d, for instance given by the molecular kinematic theory (MKT): $\cos\theta_e - \cos\theta_d = \frac{\beta}{6\mu}\dot{z}$ with β a fluid-solid friction coefficient [6]. However, experience shows that $\cos\theta_d$ differs depending on whether the fluid is advancing or retreating, which is called the *hysteresis* of the contact angle.

1.3 Capillary evolution regimes and Washburn's equation

In a very small channel, typically less than a millimetre high, the condition $\text{Bo} \ll 1$ is satisfied and the fluid flows spontaneously under the effect of capillary forces (passive microfluidics): the meniscus, whose position is marked by the coordinate $z(t)$, is subject to surface tension via Laplace pressure, and volumetric cohesion is negligible. This phenomenon does not require any external energy source, unlike an active device, and allows capillary pump systems to be constructed.

The fluid data μ_l, ρ_l and gas data μ_g, ρ_g are assumed to be constant and to verify $\mu_g \ll \mu_l$, $\rho_g \ll \rho_l$ which is the case for the water-air duality. We can assume that the upstream fluid column is laminar and follows a Hagen-Poiseuille flow profile (which demonstration in the cylindrical case is given in the appendix) with assumed constant pressures at the inlet and outlet, as well as constant contact angles with the walls equal to the equilibrium angle. For asymptotic evolution times, we obtain a regime of evolution of the meniscus position $z(t)$ called the **Lucas-Washburn regime** [7]:

$$z^2(t) = 2\frac{\sigma}{\mu}\lambda t \cos\theta_c \tag{5}$$

where $\cos\theta_c$ denotes the Cassie contact angle, defined as an average of all contact angles, and λ denotes a geometry-dependant parameter. This regime enables the definition of the *Lucas-Washburn constant* $k_{\text{LW}} := 2\frac{\sigma}{\mu}\lambda\cos\theta_c$.

In general, several successive regimes appear when filling a channel. Initially, fluid inertia dominates and the evolution is characterised by $z \propto t^2$. Then, for times greater than the initial response time $t_i = \sqrt{\rho\frac{R^3}{\sigma}}$, a classic convective regime sets in, characterised by $z \propto t$. Finally, viscous dissipation in the now longer fluid column becomes predominant, and the Washburn regime (5) sets in. This regime appears asymptotically, but in practice it is characterised by the viscous time $t_\mu = \rho\frac{R^2}{\mu}$.

1.4 Pressure evolution model

A simple model of fluid flow in a capillary network is presented by Garcia Eijo *et al* [6], based on the work of researchers at the LFD, and consists of a pressure balance in each channel of the network. Thus, for a pressure P_{in} at the inlet and P_{out} at the outlet of a channel of length L, taking into account the Laplace pressure (2) and the viscous contribution from Hagen-Poiseuille flow, we obtain **the pressure balance equation** in the channel:

$$P_{\text{out}} - P_{\text{in}} = \gamma \cos\theta_c - \rho g z - \dot{z}\kappa\left[z\mu_l + (L - z)\mu_g\right] \tag{6}$$

whose parameters κ, γ, and Cassie contact angle $\cos\theta_c$, dependent on the geometry of the section, are detailed by Garcia Eijo *et al.* [8]. As part of my learning process, I have redemonstrated this equation in the appendix for a circular section channel, starting from the equations of fluid mechanics.

1.5 Experimental method for studying particle separation using microchannels

A method developed by Garcia Eijo *et al.* [9] at the microfluidics laboratory enables the manufacturing of chips incorporating microchannels into which a fluid can be injected. This *lab-on-a-chip* method consists of integrating all the elements necessary for studying a physical phenomenon into a single system, or even to build consumer devices such as rapid medical tests. Here, a channel is cut out of adhesive or vinyl, then fixed between two previously cleaned microscope slides. The fluid is introduced into the network using a micropipette, and its filling is captured on video and processed to extract the position of the meniscus for each frame. Diffuse lighting ensures the contrast between the background and the liquid, to which a dye has been added. The advantage of this type of setup is its low cost, ease of implementation, and faster results than studies using heavy devices such as veins or pumps.

Initially designed for a comb network by Garcia Eijo *et al.* (see Section 2.2), I extended this work to T-shaped and straight channels, such as those studied subsequently. I added video options, allowing modification of colour filters and the channel to be analysed (red, green, blue or shades of grey).

1.6 Experimental measurement of fluid physical data

1.6.1 Surface tension measurement

A commonly used method for measuring the surface tension between a fluid and a surrounding gas is the hanging drop. Based on the properties of surface forces mentioned above, a drop adopts a spherical shape to minimise its interfacial energy. The experimental device, presented on Figure 4, consists of photographing a drop suspended from a needle, with the flow rate regulated by a motorised syringe pump to ensure the stability of the assembly. The *Pendant Drop* plugin for ImageJ software optimises the parameters of the analytical equation describing its surface in order to match the photograph of the drop [1], [2], and thus determine the surface tension of the fluid-gas system, as shown on Figure 5.

For distilled water with a proportion of $2/15$ black dye, the fluid used subsequently, I measured a capillary length $L_c = 1.878$ mm at a temperature of $T = 15.8$ °C and a pressure of $p = 1.005$ bar, hence $\sigma = \rho g L_c^2 = 34.6 \times 10^{-3}$ N/m. This result is close to that obtained by Garcia Eijo of 33.1×10^{-3} N/m for his $1/10$ concentration solution [9]. However, I was unable to measure this quantity at different temperatures, as the equipment at my disposal did not allow me to thermalise the fluid in the needle and syringe.

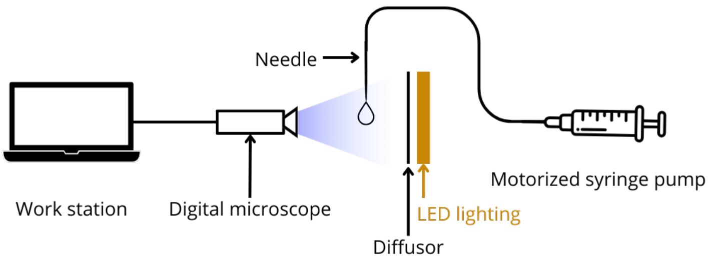

Figure 4: Experimental device used to measure σ.

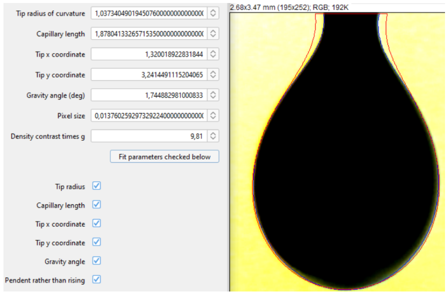

Figure 5: Photograph of a drop in the σ measurement device, with adjustment of the drop surface [1], [2].

1.6.2 Contact angle measurement

There are various methods for measuring contact angles; here, we will focus on Young's contact angle method, as it is the simplest to implement. We assume here that the surface is perfectly smooth. The experimental setup is shown in Figure 6. A drop of fluid is placed on the surface and photographed under a microscope. The contact angle is then determined by optimising the surface equation using ImageJ software and the *Drop Analysis* plugin [2], [3], as shown in Figure 7.

I measured angles of $\theta_{s,g} = 43.318\ °$ for glass and $\theta_{s,v} = 45.459\ °$ for vinyl, at a temperature of $T = 15.5\ °\text{C}$ and a pressure of $p = 1.016\ \text{bar}$. I attempted to completely thermalise the device by placing it in an oven, but the material proved unsuitable, and a Marangoni effect appeared – the drop spreading at the slightest variation in temperature. A complete device, including control of the temperature and quantity of fluid injected, also requires substantial equipment, as reported by Song *et al.* [10].

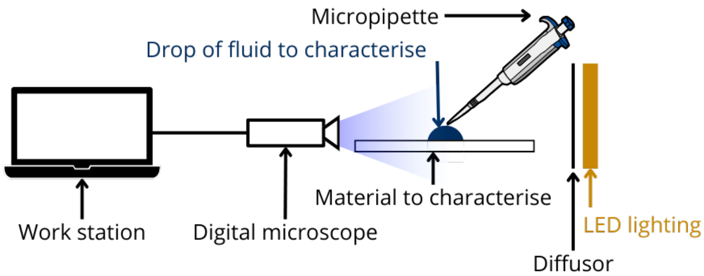

Figure 6: Experimental device used to measure θ_s.

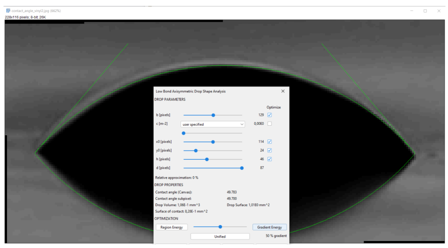

Figure 7: Photograph of a drop deposited in the θ_s measuring device, with equation adjustment [2], [3].

2 Initial studies of a uniformly heated multi-channel capillary network

The study of temperature in microfluidics opens up numerous applications: flow control and reduction of friction losses – as viscosity decreases with temperature [11], management of cooling circuits in electronics and industry [12], and assessment of blood circulation through capillary refill testing, which is influenced by temperature [13]. These principles also apply to other biological systems, such as the lungs, whose capillary networks could be better understood through a thermally controlled microfluidic approach.

Existing studies focus mainly on porous materials, often in relation to chemistry or petroleum. Bachmann *et al.* show that water content influences capillary pressure more than temperature [14], highlighting the importance of fluid properties. Li *et al.* observe an increase in height with temperature in vertical filling and explain this by adding a Boltzmann factor to the gravity-surface tension model [15]. Fang *et al.*, studying an open silicone microchannel, observe an acceleration of the dynamics up to an evaporation threshold, but still obtain the Lucas–Washburn asymptotic regime (5), suggesting universal behaviour [4].

The aim of this chapter is to study the influence of temperature on the dynamics of a fluid in comb-shaped and T-shaped capillary networks. This preliminary work will enable me to design the experimental setup and numerical treatment used throughout the internship and familiarise myself with the laboratory's microfluidic methods.

2.1 Preliminary digital study

2.1.1 Methodology

A numerical model was developed in the laboratory by Garcia Eijo [9] and adapted into MATLAB code by Thomas Duriez in a library that is currently kept private. It integrates the pressure balance equation (6) and returns the position of the meniscus $z(t)$ and the volume flow rate $Q(t)$ in each branch of a capillary network over time. I modified the code to define the physical quantities of the equation independently in each branch in order to model different temperatures. Given the difficulties mentioned in Section 1.6 in measuring these quantities, I used tabulated values, with the methodology reported in the appendix. I also implemented a visualisation utility representing a 'digital fluid' advancing according to the calculated data, to enable a qualitative comparison following the methodology of Garcia Eijo [9] and to illustrate my slideshow during my internship defence.

Initially, I studied a long straight digital channel of length $L = 80$ mm without bifurcation (not modelled by the pressure balance equation (6)), in order to observe the complete asymptotic dynamics. The temperature ranges from 20 °C to 80 °C, an interval for which the Bond number Bo is well below 1 as reported in Figure 35 in the appendix, thus placing this study in the microfluidic domain.

2.1.2 Filling dynamics

Between 20 °C and 80 °C, the capillary length L_c decreases slightly (-7%), from 2.75 mm to 2.55 mm: the gravitational contribution outweighs the capillary contribution, so that we expect to observe an acceleration of the dynamics, in agreement with the measured filling time Figure 8. Fang *et al.* also highlighted this behaviour in an open microchannel, while noting that the Lucas-Washburn asymptotic regime (5) persisted with temperature, thus postulating its universal nature [4]. The analytical formulas for the physical quantities show that an increase in temperature causes a slight decrease in surface tension but a significant decrease in kinematic viscosity. As [4] points

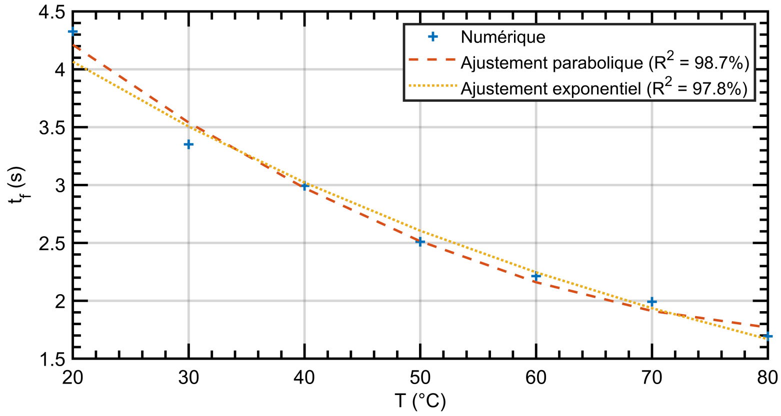

Figure 8: Filling time for the simulation.

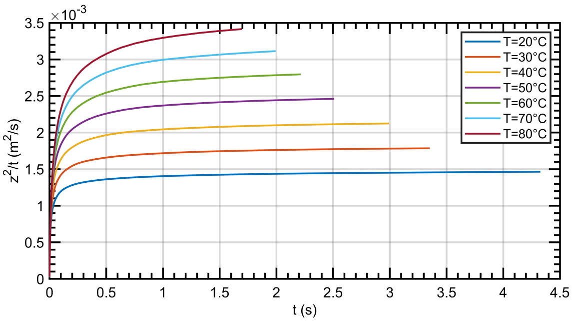

Figure 9: Change in simulated quantity z^2/t.

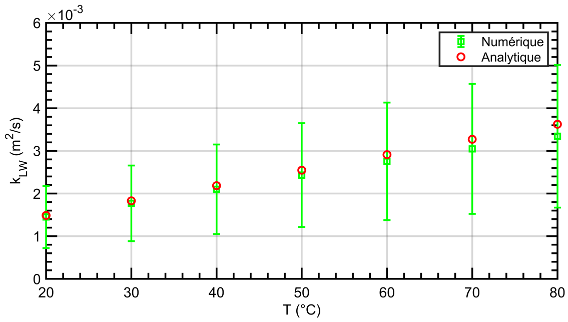

Figure 10: Lucas-Washburn constant k_{LW} of the simulation.

out, the acceleration of the fluid with temperature suggests that viscous friction forces decrease more than capillary forces: the reduction in friction largely compensates for the decrease in capillary driving force.

2.1.3 Lucas-Washburn asymptotic regime

Digital integration data can be used to study the evolution of the quantity z^2/t in order to identify the Lucas-Washburn regime. The Figure 9 shows the appearance of this regime over long periods of time. The analytical constant k_{LW} is calculated by applying (5) to the case of a rectangular cross-section channel [7], while the numerical constant is estimated by the average of the quantity z^2/t over the last five integration points. The results are presented in Figure 10, the uncertainty being estimated by the standard deviation. The numerical model correctly reproduces this constant, with the dispersion mainly resulting from the small number of points obtained from integration using the MATLAB routine `ode15s`. However, it should be noted that the Lucas-Washburn regime is asymptotic, so the constant cannot be extracted with exactitude. Finally, the increase in temperature seems to delay the establishment of this regime: the effects of inertia, which are all the more pronounced when viscosity is low, dominate over longer timescales. The analytical calculation of the characteristic times t_i and t_μ corroborates this observation.

2.1.4 Influence of pressure terms

In order to study the relative influence of viscosity and capillarity, I calculated the evolution of the corresponding pressure terms, defined from the pressure balance equation (6). The results, presented Figure 11, show that the viscous contribution remains dominant. Its relative importance increases with temperature for very short times but decreases for long times, accounting for the acceleration

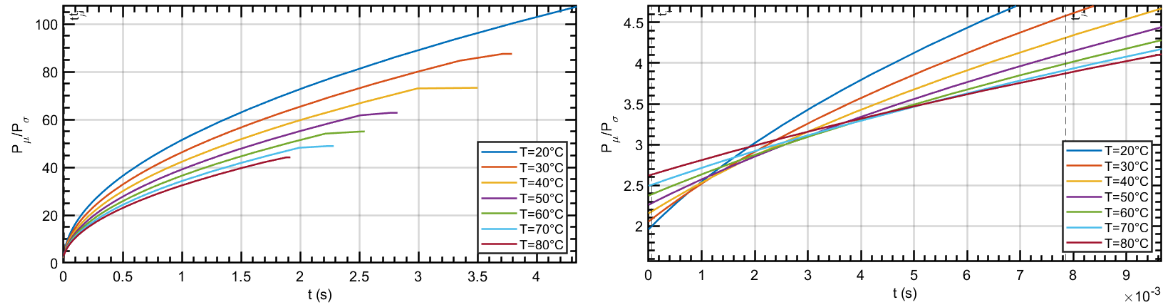

(a) Overview (b) Short-time behaviour specification

Figure 11: Ratio of pressure terms from equation (6) for numerical simulations.

of the fluid. The inertial regime thus reacts in the opposite way to the asymptotic regime, a dynamic that can be observed in the fluid velocity at short times and in the filling time. Finally, a comparison using the expressions of the forces (available in the appendix) shows that the inertial regime only manifests itself in the very first moments and is not a dominant phenomenon in the experiment.

2.1.5 Conclusions of the preliminary digital study

Based on the results of my simulations, I have conjectured for the upcoming experiments that **an increase in the temperature of the fluid introduced into the channel accelerates its dynamics**, due to the significantly greater decrease in volume and viscous forces than in surface tension action. The effects of inertia then become more significant, which may constitute a practical limitation if the channels are too short or contain irregularities. Furthermore, **the Lucas-Washburn regime should always be observed**, but with a gradual delay as the temperature increases.

2.2 Experimental methodology

2.2.1 Experimental protocol

I designed a temperature-controlled *Lab-on-a-chip* device, derived from the setup designed by Garcia Eijo *et al.* [9], shown in Figure 12. Peltier cells are placed under the chip, each controlled by a voltage generator. The temperature is measured via a Pt100 thermoresistance placed on the upper surface of the chip and connected to an Arduino board, which I wired, soldered and programmed to record data continuously. In the total thickness of the glass slide ($h_{\text{tot}} \approx 2$ mm, thermal diffusivity $\alpha \approx 0.34\ \text{mm}^2/\text{s}$), the thermal diffusion time is $t_D = h^2/\alpha \approx 11.76$ s [4], thus a longer time was allowed before each experiment to let the fluid thermalize. The temperature, pressure and humidity of air are also measured.

The first experiments, extending Garcia Eijo's study with Machine Learning ([8]), were conducted on comb and T-shaped capillary networks, illustrated in Figure 13, with 3M double-sided adhesive tape, filled with distilled water and $2/15$ black dye. Temperatures ranged from 20 °C to 80 °C, above which phase changes –or simply advection– can occur [4]. I thus carried out forty experiments, among which thirty-four are usable, for a total time comprised between fifty and sixty hours, including manufacturing, experimentation and video processing.

2.2.2 Data extraction and path analysis

Video data extraction was performed according to the method developed in Section 1.5. Following [6], I used the coefficient of determination R^2 to analyse the relevance of regressions and optimisations. I compared some experimental results with those obtained by Fang *et al.* [4], also in passive microfluidics with rough walls but in an open microchannel.

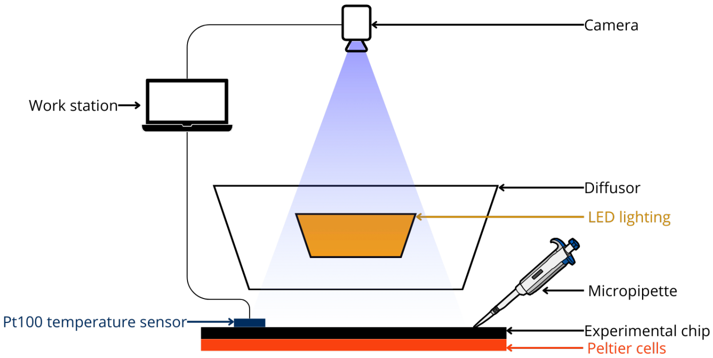

Figure 12: Experimental device used to study capillary filling under temperature control.

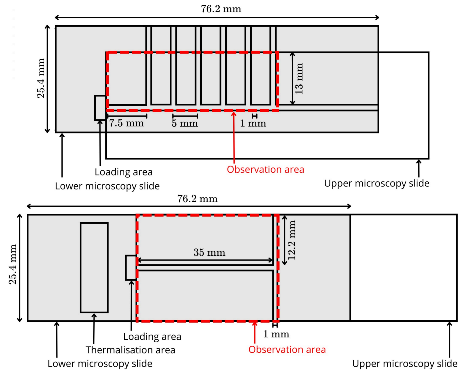

Figure 13: Diagram of chips from initial experiments with adhesive: comb-shaped (top) and T-shaped (bottom).

The position data z shows jerks and includes plateaus, or even recessions, due to the pinning-depinning phenomenon [6] as well as the video processing method, resulting in speed jumps also reported by [4]. I therefore corrected the dips and plateaus using linear interpolation. Regarding the velocity data, I experimented with the use of a digital filter using several approaches (see Figure 45 in the appendix). The filtered data appears to be the most relevant for analysing velocity alone, while I favoured the unfiltered data for calculating maximum velocity, as it best approximates the actual value according to the increment theorem.

Finally, I analysed the evolution along the paths of the comb, i.e. from the entrance of the main branch to the exit of each secondary branch, as illustrated in Figure 14. This method makes it possible to detect flow asymmetries tied to successive bifurcations.

2.3 Experimental results

2.3.1 Filling dynamics

Qualitatively, numerous jerks appear in the fluid's advance, a direct consequence of the use of adhesive. The meniscus deforms into a point that advances faster than the fluid along the walls, contradicting the theory of dynamic contact angle. These jerks seem to diminish with temperature, and the water front then appears more rectilinear, particularly near bifurcations. Figure 15 illustrates the evolution of the meniscus in the longest path (designated as path 6 in Figure 14(a)). The quantities have been made dimensionless using the path length and viscous time. We could also have used inertial time, but it is better suited to the analysis of drops and bubbles [16], and surface

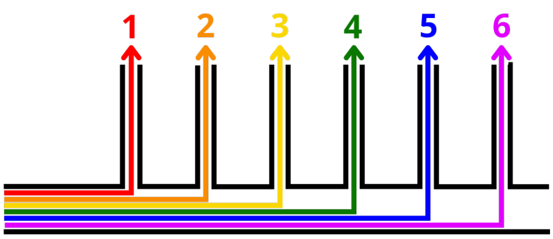

(a) Simplified diagram of channels with path identification

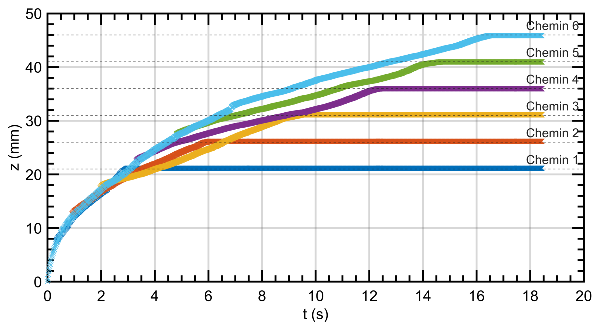

(b) Example of position data for $T = 45.71$ °C

Figure 14: Methodology for analysing paths of comb-shaped chips.

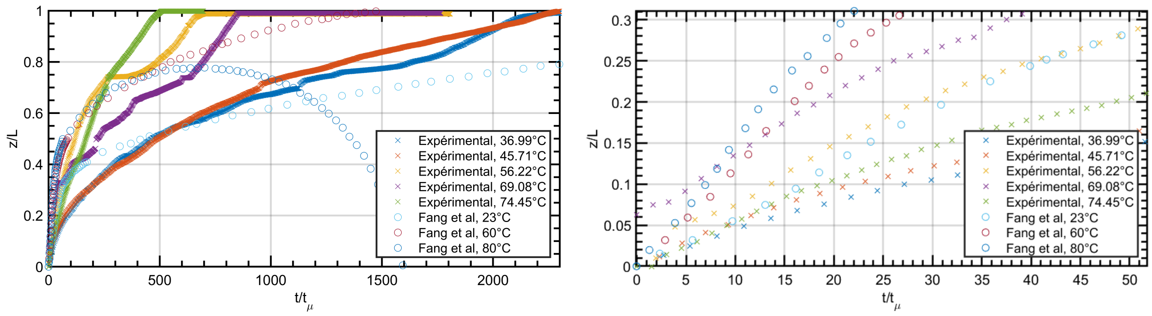

(a) Overview (b) Short-time behaviour specification

Figure 15: Evolution of the relative position in path 6 for several temperatures, and comparison with Fang *et al.* [4].

tension varies greatly in the presence of dye (see Section 3.2.2 and the measurement taken at Section 1.6.1).

At short times, the closed nature of the Fang *et al.* channel slows down the progression of the fluid, but this trend is reversed at long times. Inertia effects are therefore more significant when the channel is open, consistent with the absence of capillary forces on one of the four sides.

The filling time of paths is shown in Figure 16. The ratio $t_{f,p}/L$ increases with path length despite normalisation, which is probably explained by bifurcations: at each crossing, the fluid front splits and its dynamics are significantly slowed down. The regressions yield concave parabolas, whereas the simulation predicted convex parabolas, indicating that high temperatures induce additional effects that accelerate the dynamics. Surprisingly, the R^2 coefficient decreases with path length despite the qualitative increase in variability: the further the fluid progresses in the column, the more likely it is to be disturbed by the upstream.

The maximum velocity and the time at which it is reached are reported in Figure 17. These velocity values and the hydraulic diameter are used to calculate the Weber numbers $\mathrm{We} = \rho v_{\max}^2 D_h/\sigma \leq 0.0313 \ll 1$, which compares inertia to curvature, and the capillary number $\mathrm{Ca} = \rho\nu V/\sigma < 10^{-3} \ll 1$, which compares viscosity and curvature: over the total time of the experiment, capillary effects dominate. Almost all maximum velocities appear to be reached from the very first moment: given the very low inertial times compared to the temporal resolution ($t_i \approx 64 \quad \mu$ s), it is possible that this maximum velocity is actually reached in the inertial regime, which corroborates the initial burst phenomenon observed in [4] and is consistent with the very low value of We. Inertia should therefore not be the dominant effect on the scale of the entire experiment. Finally, the slightly increasing trend in maximum velocity (see Figure 46 in the appendix) confirms the observation made by Fang *et al.* while remaining consistent with the higher inertial contribution at short times observed in the preliminary simulation.

2.3.2 Path asymmetry and the influence of bifurcations

Following Garcia Eijo's work, I calculated the metric $J = 2\frac{t_s - t_p}{t_s + t_p}$ for each junction of the comb, where t_s and t_p denote the times at which the meniscus reaches a distance of 2.5 mm from the centre of the junction, in the secondary and main branches respectively. The experimental results are presented Figure 49 and reported in the appendix, due to excessive variability and low interpretability. Nevertheless, there is a tendency for the main branch to progress more rapidly, as the junction is not perfectly symmetrical.

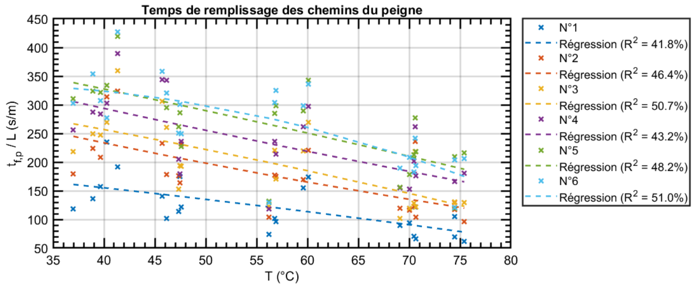

Figure 16: Path filling times, normalised by their length.

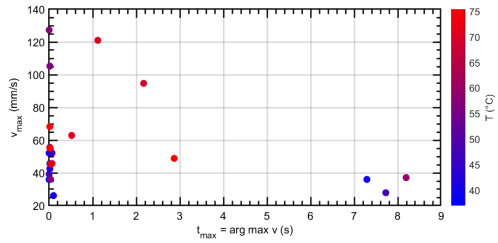

Figure 17: Maximum velocity in path 6 as a function of the time at which it is reached.

In general, variability increases significantly with temperature, but low temperatures do not reduce asymmetries, contrary to the predictions of the numerical model (see Figure 37 in the appendix). Possible explanations include the presence of right angles (rounding them would reduce asymmetry), as well as irregular edges due to the roughness of the 3M adhesive [9].

2.3.3 Dynamic Contact Angle Model (*DCAM*) optimisation

The use of 3M double-sided adhesive limits the scope of the pressure balance equation (6). Garcia Eijo *et al.* [6] developed a model known as the Dynamic Contact Angle Model (*DCAM*), where the meniscus position is optimised using numerical data:

$$z = h\left[\sqrt{2\cos\theta_{\text{eff}}\frac{\sigma t}{6\mu h} + \left(\frac{\beta_{\text{eff}}}{6\mu}\right)^2} - \frac{\beta_{\text{eff}}}{6\mu}\right] \tag{7}$$

where $\cos\theta_{\text{eff}}$ denotes the effective contact angle, and $\hat{\beta}_{\text{eff}} = \beta_{\text{eff}}/6\mu$ the effective friction coefficient. I performed this optimisation on the entire paths after trying it on individual channels, which did not work ($R^2 < 20\%$) and in any case presented a risk of overfitting, as the *DCAM* model aims to model a global evolution. I also tested an optimisation based on Garcia Eijo's effective length model l_{eff} in relation to bifurcations [9], but the results proved unsatisfactory.

The results of the DCAM optimisation are reported in Figure 48 in the appendix and compared with those obtained by Garcia Eijo *et al.* for an aspect ratio $r = w/h = 14$, which is closest to our value $r = 14.29$. Despite R^2 coefficients close to 100% (Figure 47), the optimisation cannot be considered valid due to the values $\beta_{\text{eff}} < 0$ and $\cos\theta_{\text{eff}} \ll 1$, suggesting that the optimisation has over-adjusted an unsuitable model. These observations indicate that the fluid cannot reach the asymptotic regime, as crossing a bifurcation represents an excessively large disturbance.

2.3.4 Application of different temperatures in T-branches

For the T-shaped chip shown in Figure 13(b), the analysis focuses on the heated branch compared to the cold branch. According to the preliminary simulations analysed in Section 2.1, the heated branch should fill up more quickly, although random behaviour may occur [9]. This variability, which is still an extensive research topic in microfluidics, is clearly evident in the filling times and maximum velocities, shown in Figure 50 and Figure 51 in the appendix. In theory, two branches at the same temperature should not show significant differences; however, some experiments show a filling time up to twice as short and a maximum velocity that has almost doubled. The limited number of experiments with the T-shaped chip does not allow for robust conclusions.

Qualitatively, I observed an initial phase in which the progression of the meniscus remained symmetrical in both branches. Figure 19 presents the calculation of what I defined as *symmetry time*, the interval between the start of filling a channel and the moment when the position difference

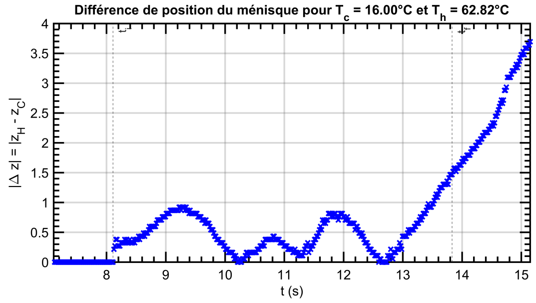

Figure 18: Example of the evolution of the difference in position in the branches of T.

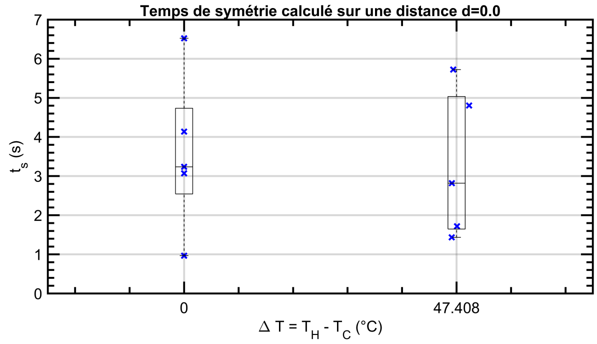

Figure 19: Symmetry time at a distance $d = 1.5$ mm.

exceeded a threshold set empirically at 1.5 mm, as illustrated Figure 18. These times are significant in relation to the analytical thermal diffusion time $t_D \approx 29.9$– 30.8 ms. At these temperature scales, the effect does not appear to be solely due to Laplace pressure, as is the case for comb-shaped chips: a Marangoni effect could occur due to heating, as suggested by simulations (see Figure 41 in the appendix).

2.3.5 Boiling phenomenon at high temperatures

At temperatures above 75 °C, bubbles form on the wall, grow larger and may or may not reach the opposite edge, as illustrated in Figure 20. In the latter case, this causes a sudden expansion upstream and downstream. Trapped between the fluid column and thin layers downstream, these bubbles slow down the progression of the fluid and can completely stop the filling process if they multiply.

This common phenomenon is called *flow boiling instability*. Bubbles form in the micro-cavities of the material and grow in the space freed up by the advancing meniscus. A criterion based on saturation pressures and temperatures can be used to predict their appearance, in accordance with the measured 75 °C: the pressure in the channel only needs to reach this threshold to trigger boiling. Humidity can also affect the evaporation of fluid [4]. The instability is described in [12] as mostly resulting from the reverse flow induced by the swelling of the bubbles, which, in our case, simply blocks the advance of the fluid. The theory applies to various channel sizes, but these observations mainly concern active flows. A detailed study would require a precise control of heat transfers, as the stability criterion is highly dependent on the heat flux q. Possible research topics include the effect of the aspect ratio r on the junction of bubbles between the walls, and the influence of roughness –which determines the size of micro-cavities– in line with the work of Garcia Eijo [9].

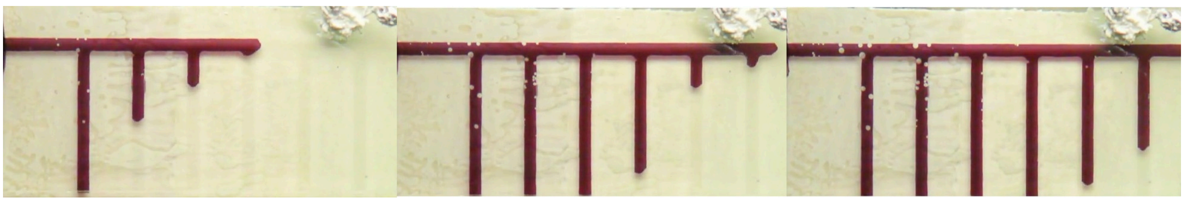

(a) $T = 74.46$ °C, $t = 2$ s (b) $T = 74, 46$ °C, $t = 5$ s (c) $T = 74.46$ °C, $t = 8$ s

(d) $T = 74.73$ °C, $t = 59$ ms (e) $T = 74.73$ °C, $t = 376$ ms (f) $T = 74.73$ °C, $t = 2.116$ s

Figure 20: Photographs of experiments illustrating stable (a–c) and unstable (d–f) bubble growth.

2.4 Limitations and conclusion

During this first part of my internship, after familiarising myself with the laboratory's methods, I designed an experimental setup to study capillary filling with temperature control. The fluid dynamics accelerate with temperature, due to a greater decrease in viscosity than in surface tension. The effects of inertia are reinforced, causing a stronger initial burst and delaying the onset of the Lucas–Washburn regime. Finally, the presence of bifurcations prevents the establishment of a clear regime and reinforces the transitional phase of the meniscus displacement.

The use of the comb-shaped chip and 3M adhesive complicated the interpretation of the results and the comparison with the digital model. The use of vinyl from the outset, as well as a simpler channel shape, would have allowed for faster model validation. The experiments also revealed considerable variability: to obtain complete data, it would be necessary to cover around ten temperatures, with fifteen tests each, as in Garcia Eijo [9] —*i.e.* nearly sixty hours for the experiments alone.

3 Study of straight channels in smooth walls heated uniformly

Given the inconclusive results of previous experiments, I decided to study a simpler system: a straight channel so as not to disrupt the dynamics, with lids made of vinyl, a material considered to be smooth [9]. After discussing this with my tutor and considering past observations, we concluded that several effects could occur at excessively high temperatures. These include increased inertia (Section 2.3.1), boiling instability (Section 2.3.5), and the Marangoni effect tied to local temperature variations.

The aim of this chapter is therefore to characterise the evolution of the fluid in this straight microchannel, subjected to a uniform temperature considered 'moderate' according to previous studies, in order to clarify the influence of temperature on dynamics and establish a basis for future experiments in the presence of thermal gradients.

3.1 Methodology

The experiments will be conducted using the experimental protocol and data processing described above, with straight-channel chips illustrated in Figure 21. Based on the conclusions of the previous study, three sufficiently low temperatures are targeted: 30 °C, 40 °C and 50 °C. These conditions allow us to focus on curvature effects while avoiding secondary phenomena at high temperatures, such as boiling, adsorption and the Marangoni effect. Three Peltier cells are used, including one for thermalisation: beyond this number, the electric current becomes too high and could damage the cables. The length of the channel studied is $L = 40$ mm. I carried out fifteen experiments, fourteen of which are usable, for a total time of approximately fifteen hours.

The thermal diffusion time in the fluid is between 52 and 54.6 ms, longer than before due to the thickness of the vinyl. To verify the thermalisation of the device, I created a digital twin on 3DExperience and simulated the steady-state thermal behaviour. The data is available in Figure 39 in the appendix. The simulated temperature of the upper wall of the channel is slightly lower than that of the lower wall due to convection with the air. A local Marangoni effect may therefore occur during the experiments.

3.2 Experimental results

The experimental data from the two tests at $T = 39.65$ °C and $T = 39.85$ °C will be discarded, as the calculated metrics proved to be anomalous and distorted the graph scales.

3.2.1 Fluid behaviour

Examples of the evolution of the meniscus position for our experiments and those of Fang *et al.* are presented in Figure 22. For similar temperatures, the dynamics are generally faster in the open channel than in the closed channel, except for $T = 51.09$ °C. However, we will see that experiments at a target temperature of 50 °C do not produce the expected effects and exhibit slower dynamics than at low temperatures, probably caused by poor thermalisation. In all cases, the progression of the meniscus is more regular than in experiments with rough walls, thanks to the use of vinyl, which allows capillarity to act more effectively.

Photos of the meniscus at different temperatures are presented Figure 23. These correspond to a position $z = 3L/4$ –in the middle of a Peltier cell to limit temperature gradients– and at a time well above the inertial time. Qualitatively, these observations confirm those made for the comb in Section 2.3.1 concerning the tip effect and the shape of the meniscus at high temperature: it is generally straighter. The use of smooth walls stabilises the advance of the meniscus, which no longer exhibits jerks (see Figure 52 in the appendix), allowing us to better interpret the data.

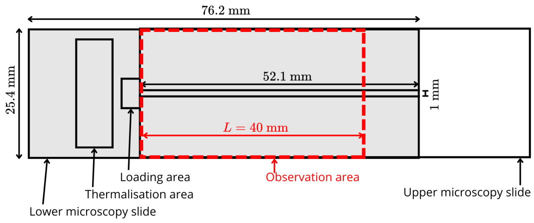

Figure 21: Diagram of the experimental straight microchannel chip with smooth vinyl walls.

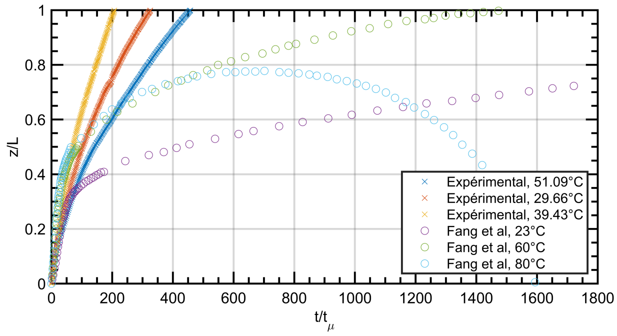

Figure 22: Examples of changes in the position of the meniscus in our experiments and those of Fang *et al.* [4].

(a) 29.66 °C (b) 30.32 °C (c) 39.43 °C (d) 48.02 °C (e) 49.80 °C (f) 51.09 °C

Figure 23: Photographs of menisci in position $z = 3L/4$.

For the rectangular channel under study, Cassie's contact angle $\cos\theta_c = \frac{h}{h+w}\cos\theta_w + \frac{w}{h+w}\cos\theta_h$ [8] allows us to determine the radius of curvature of the meniscus $R = \frac{r}{\cos\theta_c}$ [17]: an increase in the angle causes a decrease in curvature until reaching a flat meniscus. The present examples suggest that an increase in temperature decreases the contact angle, in accordance with the measurements described in Section 1.6.2.

The filling time and maximum velocity are presented Figure 53 and Figure 54 in the appendix, as they will be further analysed in the next chapter. The parabolic regression of $t_f(T)$ remains concave, so smooth walls are not sufficient to compensate for the strong inertial effects at high temperatures. According to Figure 54, the maximum velocity is still reached during the inertial regime. Here, the use of vinyl makes the variation with temperature much clearer, *i.e.* in the same direction. Smooth walls stabilise the fluid dynamics at high temperatures and allow the influence of this parameter to be better observed.

3.2.2 Optimisation of the capillary pressure term $\sigma\cos\theta$

My supervisor and I decided that the experimental manipulations required to measure the contact angle and surface tension at different temperatures could not be carried out within the scope of this internship. We decided that optimising the term $\gamma\cos\theta_c =: \sigma\cos\theta$ in the pressure balance equation (6) applied to the rectangular channel would be a first step towards a more accurate model. These two terms could then be separated after experimental measurement of $\cos\theta$, the simplest of the two. I performed the optimisation in MATLAB for times $t > 0.4$ s to avoid initial inertia effects.

The results of the optimisation are presented in Figure 24. They suggest a slight increase in the parameter between 30 °C and 50 °C, although the variability of the experiments masks the exact trend. As σ decreases with temperature, we deduce that $\cos\theta$ increases sharply, and therefore that the contact angle decreases. Experiments could confirm this intuition: heating reduces the viscosity of the fluid, promoting its spreading over the surface and thus reducing its angle (mass conservation). After testing several polynomial regressions, the second-order regression gave the best results in terms of the R^2 coefficient.

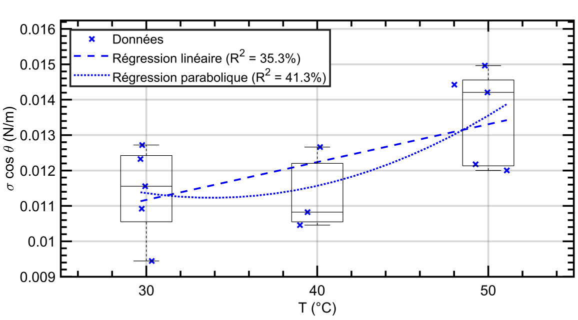

Figure 24: Optimised values of $\sigma \cos \theta$ in (6).

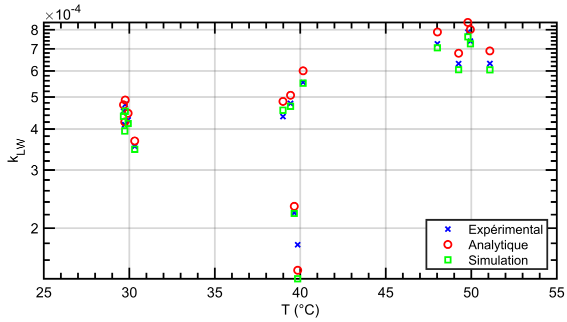

Figure 25: Lucas-Washburn constant, experimental and numerical (average), and analytical ($\sigma \cos \theta$ optimised).

3.2.3 Lucas-Washburn asymptotic regime and pressure terms

I calculated the Lucas-Washburn constant (5) using the optimised value of $\sigma \cos \theta$, while for the experimental and numerical data, I averaged the last five points of z^2/t. These three results, presented in Figure 25, agree for each experiment, suggesting the universality of the Lucas-Washburn regime conjectured in Section 2.1.3: only the analytical constant tends to slightly overestimate the other two. However, to fully observe the asymptotic regime, the channel would have to be extended.

I also used the optimised $\sigma \cos \theta$ value to compare the viscous and capillary contributions. We observe a decrease in the ratio with temperature (see Figure 56 in the appendix), consistent with the drop in viscosity, but its value is much higher than in the previous simulation (four orders of magnitude), tied to a surface tension value that is half as high. In addition, short-term dynamics, in particular the inverse variations with temperature calculated in the simulation, cannot be fully observed due to the camera's temporal resolution. Finally, it should be noted that these pressure values are not absolute, as they are derived from a numerical optimisation.

3.3 Limitations and conclusion

The use of vinyl to manufacture straight-channel chips has enabled more robust conclusions to be drawn about the dynamics of uniformly heated fluid. Compared to the initial experiments, inertial effects and acceleration of the dynamics are observed more markedly. Optimisation of the parameter $\sigma \cos \theta$ has outlined a universality of the Lucas-Washburn regime, already described by Fang *et al.* [4], but remains a conjecture.

However, the experiments at a target temperature of $50°C$ seem aberrant: the thermalisation of the fluid may have been imperfect, or unprojected physical effects, such as a Marangoni flow, may have taken place. Furthermore, the fluid does not follow the tabulated values of the physical quantities, in particular σ. To characterise this fluid at different temperatures, a precise study with perfect thermalisation would be necessary, as explained in Section 1.6.2. Even a small amount of dye acts as a surfactant, strongly affecting the surface tension.

Finally, the channel remains too short to observe an asymptotic regime, limited by the size of the chip (25.4 mm). Adding curves to extend its total length would however cause other slowing effects and require new models, studied in depth by Garcia Eijo [9].

4 Study of straight channels with smooth walls in the presence of temperature gradients

In the litterature, the Marangoni effect is usually studied on free surfaces (*i.e.* in transverse dynamics) rather than in filling. The induced convection is well known, for example when different temperatures are set at both ends of a fluid surface [18]. Azese *et al.* developed a heuristic model describing the temporal evolution of surface tension along a channel and its effects on pressure terms, compensating for the absence of inertia in Lucas-Washburn's theory [16]. Finally, the value of the surface tension gradient seems to matter more than the value itself [19].

The objective of this chapter is to study the straight microchannel presented in Section 3, here imposing temperature gradients. We are thus working within the domain of thermocapillarity, where the variation of surface tension results from a thermal gradient rather than a concentration of surfactants.

4.1 Methodology

4.1.1 Modification of the theoretical framework in the presence of gradients

We can no longer use the pressure balance equation (6), which is based on the assumption of constant surface tension and does not take into account any induced inertia effects [16]. Furthermore, according to the expression of the Marangoni force (3), this effect is tangential and acts on the liquid-gas interface: a fluid rolling effect therefore occurs in the channel, as illustrated in Figure 26. Furthermore, this rolling mathematically generates an additional Marangoni effect (*self-induced Marangoni effect*) through the simple movement of the contact line [20].

According to an analysis of physical quantities using the Vaschy-Buckingham theorem (reported in the appendix), two dimensionless numbers can be used to characterise fluid flow in a parallelepiped channel of length L. The **Prandtl number** $\mathrm{Pr} = \frac{\mu}{\rho\alpha}$, where α denotes the thermal diffusivity of the liquid, compares the time scales of thermal and viscous diffusion. The **Marangoni number** $\mathrm{Ma} = \frac{\partial\sigma}{\partial T}\frac{L\Delta T}{\mu\alpha}$, where ΔT denotes the temperature difference between the two ends and $\frac{\partial\sigma}{\partial T}$ the resulting surface tension gradient, compares the advective transport due to surface tension with thermal diffusive transport. To simplify the analytical calculation, we will assume a linear evolution of quantities along the channel: $\frac{\partial\sigma}{\partial T} \approx \frac{\Delta\sigma}{\Delta T}$. If $|\mathrm{Ma}| \gg 1$, the flow is said to be dominated by the gradient, otherwise only thermal diffusive transport remains.

During this internship, I was unable to develop a complete theoretical model, which would have required adapting the concept of dynamic contact angle to gradients. My modelling attempt is included in the appendix. In the end, I simply added a term $-\partial_z\sigma$ to the pressure balance equation (6) and adapted the numerical integration of Thomas Duriez's code to include position-dependent physical values. The modified equation is:

(a) Favourable gradient $\partial_z\sigma > 0$ (b) Adverse gradient $\partial_z\sigma < 0$

Figure 26: Diagram of thermocapillarity in a microchannel: (1) Marangoni force, (2) particle movement at the interface, (3) propagation along the wall.

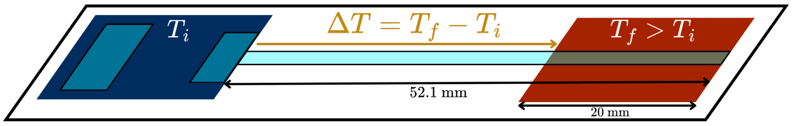

Figure 27: Simplified diagram of the experimental setup for studying filling under temperature gradients.

$$P_{\text{out}} - P_{\text{in}} = \gamma \cos \theta_c - \frac{\partial \sigma}{\partial z} - \rho g z - \dot{z} \kappa \left[z \mu_l + (L - z) \mu_g \right)] \tag{8}$$

However, this approach assumes a constant contact angle and that the gradient does not influence the other terms of the equation. Other thermal effects may also come into play in addition to the Marangoni force. If the aim is to isolate the latter, it would be preferable to use a variation in surfactant concentration, which would allow the characteristic velocity $u \approx (\Delta\sigma)/\mu$ resulting from the Marangoni number Ma to be observed.

4.1.2 Experimental protocol

The experimental setup presented in Section 1.5 is adapted by positioning two Peltier cells heated at different temperatures, and spaced apart by a distance $L = 32.1$ mm, as illustrated in Figure 27. I tested three types of gradients (30– 50°C, 40– 50°C, and 30– 40°C), whose limits correspond to the temperatures studied in the straight channel under uniform heating in Section 3. I conducted fifteen experiments, for a total time of about twenty hours.

To simplify the analysis, I modelled the surface tension as linear with temperature, a common practice in studies on the Marangoni effect, as done by Farahi *et al.*, who placed air pockets at regular intervals to force this effect [21]. Amador *et al.* also used this model for straight channels of similar dimensions, with gradients imposed by Peltier cells [22]. However, we cannot compare our results with theirs, which were obtained using active microfluidics.

4.1.3 Numerical simulation of the modified equation

The pressure balance equation with the gradient term (8) was solved numerically for the types of temperature gradients described above. The results are presented Figure 28.

According to the dynamics Figure 28(a), the channel filling times vary little between these different thermal loadings, due to the small temperature range (30– 50 °C) and the short channel length used. Fluids subjected to a gradient accelerate after a certain time. For example, the fluid under loading $T_i = 30$ °C, $T_f = 50$ °C is initially behind the fluid subjected to the uniform temperature $T = 40$ °C, but eventually catches up. The Lucas-Washburn regime is therefore not reached until the surface tension has stabilised. The importance of the gradient described in [19] seems to be verified, even if the assertion that it is *“more important than the value itself”* remains to be discussed with the experimental data.

Finally, according to the capillary pressures Figure 28(b), the adverse gradient produces a slowdown in dynamics, which is clearly observable when comparing the experiment under thermal loading 30°C → 50°C with that at a uniform temperature of 50 °C: the fluid at a uniform temperature eventually catches up with the other.

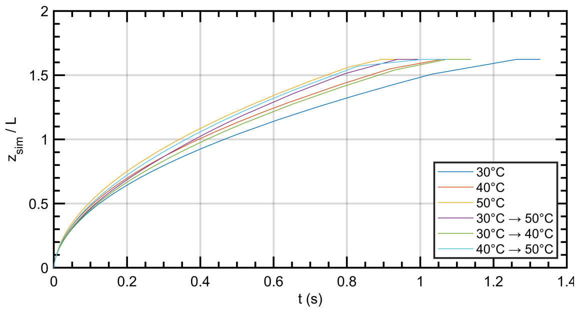

(a) Simulated position of the meniscus

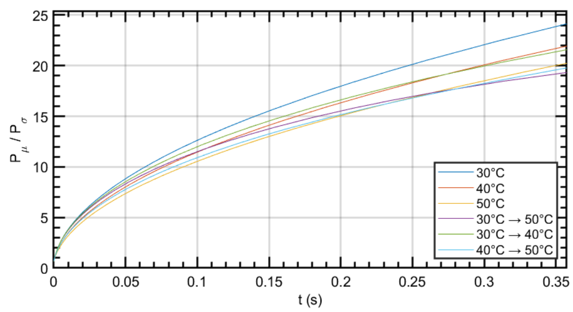

(b) Ratio of viscous and capillary pressure terms

Figure 28: Result of the numerical integration of the modified pressure balance equation (8) depending on the thermal loading.

4.2 Experimental results

4.2.1 Characterisation of experiments and dimensionless numbers

The numbers calculated for our experiments are presented Figure 57 in the appendix. The Marangoni number Ma is very high, indicating that the flow is dominated by the surface tension gradient. The Prandtl number Pr is also high, which means that thermal diffusion prevails over viscous diffusion in the fluid. Finally, these two numbers differ significantly depending on the thermal loading, even when the gradients ΔT are identical. They cannot be linked *a priori* by a closed formula, so it is still necessary to use both to characterise the experiments, as predicted by the Vaschy-Buckingham theorem.

4.2.2 Meniscus shape and filling dynamics

Following on from the work of Garcia Eijo *et al.* [6], I used Surface Evolver to simulate the surface of the meniscus [23]. The complete methodology is presented in the appendix. Figure 29 compares a simulated surface—assuming a linear temperature variation and a constant contact angle—with photographs of the meniscus from an experiment at the same positions. According to the digital model, the maximum curvature of the meniscus is located between the vertical walls, which cannot be observed experimentally due to the placement of the camera: the effect of temperature will therefore be less obvious in the images. In addition, the model appears limited, showing no significant variations in shape with surface tension. This is directly related to the calculation method of Surface Evolver, which imposes a contact angle and then optimises the rest of the surface. I nevertheless spent many hours adjusting the model, but I did not have time to correct the defect in the upper right contact line, which contradicts the observations of Garcia Eijo [9].

As it moves through the channel, the actual meniscus appears to flatten as the temperature increases, consistent with observations at uniform temperature Section 3.2.1. However, we do not observe any significant changes in the shape of the meniscus in the presence of gradients —apart from the usual variability— showing that the Marangoni effect remains weak in these experiments.

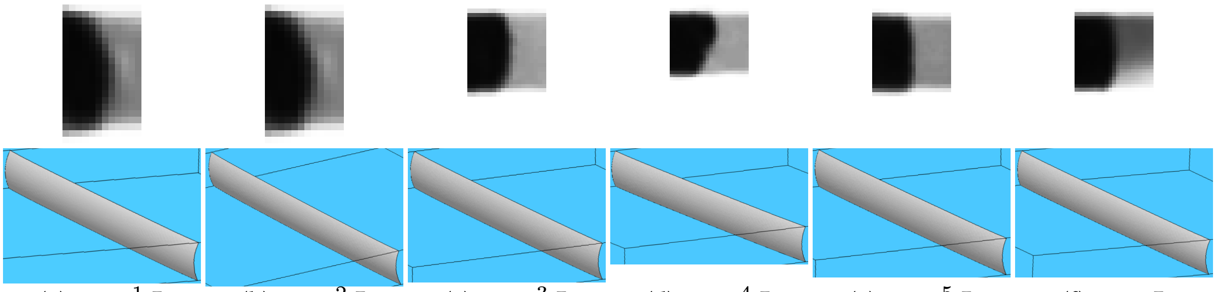

(a) $z = \frac{1}{6}L$ (b) $z = \frac{2}{6}L$ (c) $z = \frac{3}{6}L$ (d) $z = \frac{4}{6}L$ (e) $z = \frac{5}{6}L$ (f) $z = L$

Figure 29: Photographs of the meniscus shape at different positions for $\mathrm{Pr} = 4.77$, $|\mathrm{Ma}| = 4.68 \times 10^5$, compared to modelling on Surface Evolver.

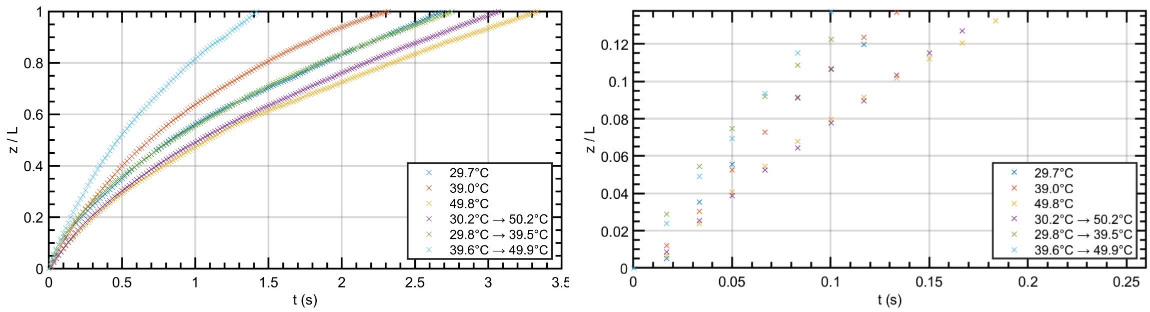

(a) Overview (b) Short-time behaviour specification

Figure 30: Change in the relative position of the meniscus depending on thermal loading.

Examples of changes in the position of the meniscus are shown in Figure 30. In the presence of a gradient, a higher inlet temperature does not necessarily lead to a greater initial burst: the intuitive prediction is not verified here. When comparing a uniform temperature with a gradient, the dynamics of the fluid subjected to the gradient appear slower than those of the fluids in channels uniformly heated at T_i and T_f. In addition, a stronger gradient tends to slow down the fluid, illustrating the adverse effect of the surface tension gradient. Finally, for two equal gradients ($\Delta T = 10$ °C), a higher overall temperature accelerates the fluid, highlighting the importance of the two dimensionless numbers Ma and Pr for the analysis: the Marangoni number captures the effect of the gradient —the stronger it is, the more the flow slows down— while the Prandtl number reflects the importance of the overall value —the greater it is, the more the flow accelerates— contradicting the statement presented in [19].

4.2.3 Filling time and maximum velocity

Filling times and maximum velocities are shown in Figure 31 and Figure 32, excluding outliers ($t_f > 5$ s). The variation in filling time heavily depends on the type of thermal load. For two equal gradients ($\Delta T = 10$ °C), the average time for the lowest temperatures ($|\mathrm{Ma}| \approx 4.69 \times 10^5$) is 2.65 higher than for the highest ($|\mathrm{Ma}| \approx 5.75 \times 10^5$). This effect is also noticeable when comparing the gradients 30 °C → 50 °C and 40 °C → 50 °C, which can be interpreted by the lower initial temperature of one of the two.

Finally, according to Figure 32, the initial burst is always observed even in the presence of a gradient, indicating that the Marangoni effect remains negligible compared to inertia at short times. However, for the same initial temperature T_i, the maximum velocity appears slightly higher with a gradient, which seems counterintuitive compared to the expected adverse effect of the surface tension gradient.

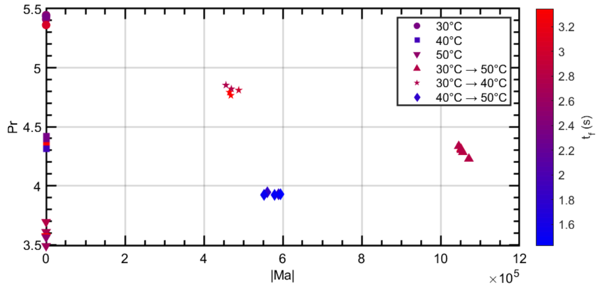

Figure 31: Filling time for the section with length $L = 32.1$ mm depending on the thermal loading.

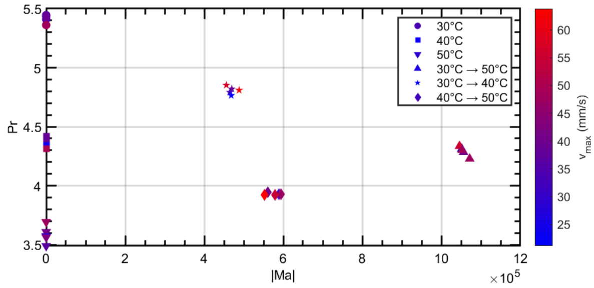

Figure 32: Maximum velocity in the section with length $L = 32.1$ mm depending on the thermal loading.

4.2.4 Optimisation of the modified pressure balance equation (8)

To verify the modified pressure balance equation (8), I performed a numerical optimisation of the gradient term by applying the routine described in Section 3.2.2. I used a parabolic interpolation of $(\sigma \cos \theta)(T)$ and the temperature modelling from 3DExperience, which proved to be more accurate than the linear approximation. Since the variation in $\sigma \cos \theta$ is negligible for similar temperatures, I only performed one CAD simulation per type of thermal loading.

Figure 33 presents an example of an optimised equation, whose relevance is qualitatively determined as *average*. Two other examples, presented in Figure 59 in the appendix, illustrate the best and worst fits, respectively. The optimised gradient values are reported Figure 34, and the R^2 coefficients are shown in Figure 60 in the appendix. In general, the discrepancies stem from actual dynamics that are slower than those predicted by the model, which shows that equation (8) does not capture all the effects related to the gradient.

By calculating the gradient analytically and using it as the initial condition for optimisation, I observed, surprisingly, that it often constituted a local minimum of the expression (8). In this case, the MATLAB routine did not need to optimise it and produced excellent correlations ($R^2 > 99\%$). Conversely, when the optimisation deviated from this analytical value, the results were mediocre ($R^2 < 70\%$) or even aberrant ($R^2 < 0$). We can conclude that these observations are either a coincidence or the result of poor modelling of the temperature or the coefficient $\sigma \cos \theta$, leading to aberrant results.

4.3 Limitations and conclusion

This last series of experiments has provided initial observations on the influence of a temperature gradient on the evolution of a fluid in a microchannel. The Marangoni number Ma and the Prandtl

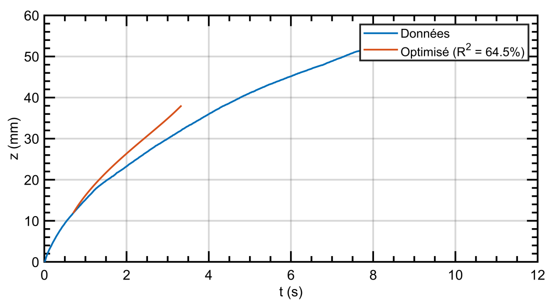

Figure 33: Example of optimisation of the modified pressure balance equation (8).

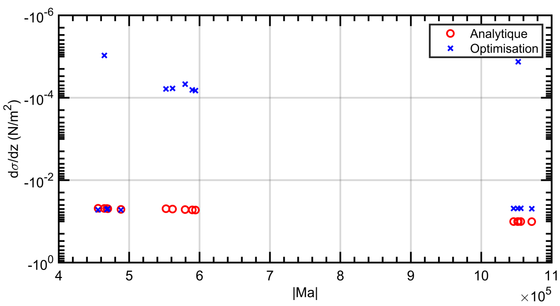

Figure 34: Optimised values of $\partial_z \sigma$ in (8), using the interpolation of $\sigma \cos \theta$.

number Pr jointly characterise the experiments and cannot be separated for the establishment of a theoretical model: while one accounts for the effect of the gradient, the other reflects the value of the temperature itself. The addition of a gradient term $\partial_z \sigma$ to the pressure balance equation (6) seems to partially take into account the Marangoni effect, but further experiments are needed to validate this approach. Furthermore, the modified equation (8) is not based on a correct physical demonstration, and the quality of the optimisation depends heavily on the modelling of the temperature and the term $\sigma \cos \theta$.

Despite the use of a simple channel with smooth walls, many experimental challenges remain, including significant variability. As the simulation shows, Peltier cells do not heat the chip perfectly, particularly due to convection with the air. Solutions would include the use of insulating materials around the chip or the addition of cells at different points, but this could significantly alter the way video data is acquired if the chip became partially obstructed.

Conclusion

Learning of investigations techniques

This internship allowed me to discover microfluidics and capillary effects, which I was introduced to during my preparation for the International Physicists' Tournament (IPT) and explored in greater depth during this experience. The highly experimental nature of the work led me to develop my manual skills —as well as my patience— and to acquire knowledge in related fields such as electronics and soldering. Although my theoretical calculations remain incomplete, the tests carried out have reinforced my interest in model development and optimisation.

Challenges faced

Despite numerous checks, heat transfer remained imperfect, affected by chip-resistance contact and the bilateral sensitivity of the thermoresistance, so that a discrepancy persisted even with thermal paste. The Peltier effect, inducing a current when its two sides were at different temperatures, caused significant time drift. The experiments therefore took much longer than expected.

The temperature control system underwent numerous iterations, often unsuccessful. The initial objective was to use a relay for control, but the available equipment did not allow for high currents. It was not possible to fully characterise the Peltier cells (voltage-temperature and current-temperature curves) due to excessive variability between tests; however, partial data is available in the appendix for future use.

Given the complexity of modelling the meniscus with the Marangoni effect, I had considered using the Lattice-Boltzmann method to simulate the entire flow. After studying the modalities, I quickly realised that this would take too much time and therefore abandoned this approach.

Outlook

This work opens up numerous possibilities for the separation of fluids by thermal control, which until now has been applied via walls, and can be explored individually or holistically. This report will therefore contribute to the research of several doctoral students at the laboratory who are already working on thermal variations.

Although the study focused on longitudinal surface tension gradients, transverse gradients could generate even more pronounced Marangoni effects, as the temperature variation is greater on the surface. The aspect ratio, already studied by Garcia Eijo and generally considered a key parameter, could constitute an additional axis for developing a model of evolution in the presence of temperature and surface tension gradients [9], [16].

Glossary

Contact angle (θ): Angle formed by a drop of liquid with a solid surface, characterising wetting (hydrophilic if $< 90°$, hydrophobic if $> 90°$).

Cassie contact angle (θ_c): Average contact angle taking into account the geometry of the channel and the different surfaces in contact.

Dynamic contact angle (θ_d): Contact angle of a fluid in motion, generally different from the pressure balance angle.

Bond number (Bo): Dimensionless number comparing gravitational forces to surface tension forces ($\mathrm{Bo} < 1$ in microfluidics).

Capillarity: Physical phenomenon allowing a liquid to rise or fall in a thin tube under the effect of surface tension.

Peltier cell: Thermoelectric device used to heat or cool a surface by applying an electric current.

Capillary number (Ca): Dimensionless number comparing viscous forces to surface tension forces.

Curvature: Measure of the deformation of a surface relative to a plane.

DCAM (*Dynamic Contact Angle Model*): Theoretical model describing the evolution of the contact angle of a moving fluid, developed by Garcia Eijo.

Hydraulic diameter: Characteristic dimension of a non-circular channel, calculated from its cross-sectional area.

Thermal diffusivity: Property of a material characterising the speed at which heat propagates within it.

Hagen-Poiseuille flow: Laminar flow of a viscous fluid in a cylindrical tube, with a parabolic velocity profile.

Marangoni effect: Tangential force created by a surface tension gradient, causing fluid movement.

Flow boiling instability: Flow instability caused by the formation of vapour bubbles at high temperatures.

Hydrophilic: Property of a surface that attracts water (contact angle $\theta < 90°$).

Hydrophobic: Property of a surface that repels water (contact angle $\theta > 90°$).

Lab-on-a-chip: Technique that miniaturises laboratory processes onto a single chip measuring a few centimetres.

Lucas-Washburn regime: Relationship describing the progression of a fluid in a capillary channel (square position proportional to time).

Capillary length: Characteristic distance comparing the effects of surface tension to those of gravity.

Marangoni number (Ma): Dimensionless number characterising the importance of the Marangoni effect relative to thermal diffusion.

Meniscus: Curved interface between a liquid and a gas in a channel, whose shape depends on the contact angle.

Microfluidics: Field of fluid mechanics studying flows in micrometric channels.

Passive microfluidics: Microfluidic system operating without an external energy source, using only capillary forces.

Pinning-depinning: Phenomenon of the contact line sticking to and then detaching from surface defects.

Laplace pressure: Overpressure inside a curved interface, proportional to surface tension and curvature.

Prandtl number (Pr): Dimensionless number comparing viscous diffusion to thermal diffusion.

Chip: Miniaturised device, in this case containing micrometric channels for manipulating fluids.

Asymptotic regime: Long-term behaviour of a system.

Inertial regime: Initial phase of flow where inertial forces dominate (high acceleration).

Viscous regime: Phase of flow where viscous forces dominate (due to friction between the fluid and the wall).

Surfactant: Substance that reduces the surface tension between two phases (such as soap in water).

Surface tension (σ): Force exerted at the interface between two phases, tending to minimise the contact area.

Thermocapillarity: Variation in surface tension due to a temperature gradient, source of Marangoni effects.

Thermal resistance: Electrical component whose resistance, measured in ohms, varies with temperature.

Viscous time: Characteristic time for establishing viscous flow in a capillary flow.

Vinyl: Smooth material generally with one adhesive side and one side that becomes adhesive through lamination (high-temperature compression).

Dynamic viscosity (μ): Property of a fluid characterising its resistance to flow.

Weber number (We): Dimensionless number comparing inertial forces to surface tension forces.

Bibliography

[1] A. Daerr and A. Mogne, 'Pendent_Drop: An ImageJ Plugin to Measure the Surface Tension from an Image of a Pendent Drop', *Journal of Open Research Software*, Jan. 2016, doi: 10.5334/jors.97.

[2] J. Schindelin *et al.*, 'Fiji: an open-source platform for biological-image analysis', *Nature Methods*, vol. 9, no. 7, pp. 676–682, Jul. 2012, doi: 10.1038/nmeth.2019.

[3] A. Stalder, G. Kulik, D. Sage, L. Barbieri, and P. Hoffmann, 'A snake-based approach to accurate determination of both contact points and contact angles', *Colloids and Surfaces A: Physicochemical and Engineering Aspects*, vol. 286, no. 1, pp. 92–103, 2006, doi: https://doi.org/10.1016/j.colsurfa.2006.03.008.

[4] R. Fang *et al.*, 'Temperature Effect on Capillary Flow Dynamics in 1D Array of Open Nanotextured Microchannels Produced by Femtosecond Laser on Silicon', *Nanomaterials*, vol. 10, no. 4, 2020, doi: 10.3390/nano10040796.

[5] C. O. POPIEL and J. WOJTKOWIAK, 'Simple Formulas for Thermophysical Properties of Liquid Water for Heat Transfer Calculations (from 0°C to 150°C)', *Heat Transfer Engineering*, vol. 19, no. 3, pp. 87–101, 1998, doi: 10.1080/01457639808939929.

[6] P. M. Garcia Eijo, J. M. Cabaleiro, and G. Artana, 'Capillary Flow Dynamics in Composite Rectangular Microchannels with Rough Walls', *Langmuir*, vol. 38, no. 43, pp. 13296–13304, Nov. 2022, doi: 10.1021/acs.langmuir.2c02496.

[7] J. Berthier, D. Gosselin, and E. Berthier, 'A generalization of the Lucas–Washburn–Rideal law to composite microchannels of arbitrary cross section', *Microfluid. Nanofluidics*, vol. 19, no. 3, pp. 497–507, Sep. 2015, doi: https://doi.org/10.1007/s10404-014-1519-3.

[8] P. M. Garcia Eijo, T. Duriez, J. M. Cabaleiro, and G. Artana, 'A machine learning-based framework to design capillary-driven networks', *Lab Chip*, vol. 22, no. 24, pp. 4860–4870, 2022, doi: 10.1039/D2LC00843B.

[9] P. M. García Eijo, 'Desarrollo y caracterización de sistemas de bombeo pasivo por capilaridad utilizando tecnología microfluídica de bajo costo para ser empleado en dispositivos Lab-on-a-Chip', 2025.

[10] J.-W. Song and L.-W. Fan, 'Temperature dependence of the contact angle of water: A review of research progress, theoretical understanding, and implications for boiling heat transfer', *Advances in Colloid and Interface Science*, vol. 288, p. 102339, 2021, doi: https://doi.org/10.1016/j.cis.2020.102339.

[11] K. Lucas, 'Ein einfaches Verfahren zur Berechnung der Viskosität von Gasen und Gasgemischen', *Chemie Ingenieur Technik*, vol. 46, no. 4, p. 157, 1974, doi: https://doi.org/10.1002/cite.330460413.

[12] S. Kandlikar, 'Chapter 5. Flow Boiling in Minichannels and Microchannels', 2006, pp. 175–226. doi: 10.1016/B978-008044527-4/50007-4.

[13] D. L. Schriger and L. Baraff, 'Defining normal capillary refill: variation with age, sex, and temperature', *Ann. Emerg. Med.*, vol. 17, no. 9, pp. 932–935, Sep. 1988, doi: 10.1016/s0196-0644(88)80675-9.

[14] J. Bachmann, R. Horton, S. A. Grant, and R. R. van der Ploeg, 'Temperature Dependence of Water Retention Curves for Wettable and Water-Repellent Soils', *Soil Science Society of America Journal*, vol. 66, no. 1, pp. 44–52, 2002, doi: https://doi.org/10.2136/sssaj2002.4400.

[15] X.-X. Li *et al.*, 'Temperature-dependent capillary rise and its effects on fabric cleaning and permeability', *Therm. Sci.*, vol. 27, no. 3 Part A, pp. 1915–1920, 2023.

[16] M. N. Azese, J. J. Engola, J. Hona, E. Jean Yap, and Y. C. Mbono Samba, 'Examining capillary dynamics in rectangular and circular conduits subject to unsteady surface tension', *Journal of Fluid Mechanics*, vol. 949, p. A6, 2022, doi: 10.1017/jfm.2022.729.

[17] H. Bruus, *Theoretical Microfluidics*. 2008, p. . doi: 10.1093/oso/9780199235087.001.0001.

[18] E. Chen and F. Xu, 'Transient Marangoni convection induced by an isothermal sidewall of a rectangular liquid pool', *Journal of Fluid Mechanics*, vol. 928, p. A6, 2021, doi: 10.1017/jfm.2021.795.

[19] S. H. Davis, A.-K. Liu, and G. R. Sealy, 'Motion driven by surface-tension gradients in a tube lining', *J. Fluid Mech.*, vol. 62, no. 4, pp. 737–751, Feb. 1974.

[20] J. J. Thalakkottor and K. Mohseni, 'The role of surface tension gradient in determining microscopic dynamic contact angle'. [Online]. Available: https://arxiv.org/abs/1803.05931

[21] R. H. Farahi, A. Passian, T. L. Ferrell, and T. Thundat, 'Microfluidic manipulation via Marangoni forces', *Applied Physics Letters*, vol. 85, no. 18, pp. 4237–4239, Nov. 2004, doi: 10.1063/1.1812830.

[22] G. J. Amador, A. F. Tabak, Z. Ren, Y. Alapan, O. Yasa, and M. Sitti, 'Thermocapillary-driven fluid flow within microchannels'. [Online]. Available: https://arxiv.org/abs/1802.00475

[23] K. A. Brakke, 'The Surface Evolver', *Experimental Mathematics*, vol. 1, no. 2, pp. 141–165, 1992, doi: 10.1080/10586458.1992.10504253.

[24] N. Aeronautics and S. F. Space Administration (NASA) Air Viscosity, [Online]. Available: https://www.grc.nasa.gov/www/k-12/airplane/viscosity.html

[25] N. B. Vargaftik, B. N. Volkov, and L. D. Voljak, 'International Tables of the Surface Tension of Water', *Journal of Physical and Chemical Reference Data*, vol. 12, no. 3, pp. 817–820, Jul. 1983, doi: 10.1063/1.555688.

[26] T. Blake and J. Haynes, 'Kinetics of liquidliquid displacement', *Journal of Colloid and Interface Science*, vol. 30, no. 3, pp. 421–423, 1969, doi: https://doi.org/10.1016/0021-9797(69)90411-1.

[27] N.-A. Goy, N. Bruni, A. Girot, J.-P. Delville, and U. Delabre, 'Thermal Marangoni trapping driven by laser absorption in evaporating droplets for particle deposition', *Soft Matter*, vol. 18, no. 41, pp. 7949–7958, 2022, doi: 10.1039/D2SM01019D.

Appendix

I Internship schedule

Week of May 26, 2025 • Documentation on thermocapillarity • Getting started with the digital library • Training in protocols: chip manufacturing, assembly, data processing	**Week of June 2, 2025** • Bibliography on capillarity and thermocapillarity • Learning the basics of capillarity • Receiving and soldering electronic components
Week of June 9, 2025 • Chip manufacturing • Arduino programming for thermal resistance • Creation of a digital twin of the experiments in 3DExperience	**Week of June 16, 2025** • Arduino programming for relay use • Theoretical calculations on Poiseuille flow and the pressure balance equation
Week of June 23, 2025 • Data processing code: interpolations (l_{eff} [9], DCAM [6]) • Attempts to manipulate the electrical relay • Documentation on local temperature control	**Week of June 30, 2025** • Experiments using 3M adhesive chips (comb, T) • Processing of corresponding video data
Week of July 7, 2025 • Initial interpretations of experiments using adhesive • Documentation on the boiling effect	**Week of July 14, 2025** • Documentation on the Marangoni effect • Theoretical calculations for modelling the Marangoni effect • Surface Evolver simulations
Week of July 21, 2025 • Chip manufacturing • Numerical simulation tests using the Lattice-Boltzmann method • Implementation of protocols for measuring contact angle and surface tension	**Week of July 28, 2025** • Experiments using the smooth straight channel at uniform temperatures • Processing of corresponding video data • Understanding and modifying Thomas Duriez's code to integrate temperature variations
Week of August 4, 2025 • Optimisation of $\sigma \cos\theta$ for the straight channel • Experiments using the smooth straight channel with temperature gradients • Processing of corresponding video data	**Week of August 11, 2025** • Calculation of metrics and formatting under graphs • Drafting of physical interpretations and comparisons • Drafting of the report
Week of August 18, 2025 • Optimisation of $\partial_z \sigma$ for the straight channel • Attempt to measure the contact angle under thermalisation • Correction of numerical simulations of the meniscus using Surface Evolver • Drafting of the report	

II Theoretical background

II.1 Formulas used to calculate physical quantities as a function of temperature

- The air is assumed to be dry and its viscosity is calculated using Sutherland's formula: $\mu_g(T) = \mu_{g,0}\left(\frac{T}{T_0}\right)^{3/2}\frac{T_0+S}{T+S}$ with $S = 113$ K, and a reference $\mu_{g,0} = 1.825 \times 10^{-5}$ Pa.s at $T_0 = 20$ °C, under a pressure close to 1 atm $= 1.013$ bar [24];
- Surface tension σ is calculated using the expression given by [25], itself obtained by interpolation of experimental tables;
- The density of water ρ is interpolated from [5], depending on temperature and pressure;
- The viscosity of water μ_l is calculated according to Lucas' formula [11], depending on temperature and pressure;
- The contact angle $\cos\theta$, which is difficult to measure according to Section 1.6.2, was initially assumed to be constant, in accordance with the observations of Song *et al.* for the interval 20– 80 °C [10]. In the MATLAB code developed at the laboratory, Thomas Duriez set them for the top/bottom and side walls to $\theta_h = 24.9867°$ and $\theta_w = 79.9620°$, respectively.

II.2 Demonstration of the pressure balance equation (6) in a circular cross-section channel

Consider a channel of length L and circular cross-section S with radius R. We will use cylindrical coordinates and assume a real Newtonian fluid. The fluid is assumed to flow through the channel at a longitudinal velocity that is invariant under rotation, i.e. $\vec{v} = v(r)\vec{e_z}$. The position of the meniscus is marked by the coordinate z, with the fluid denoted by the index l being upstream and the ambient air denoted by the index g being downstream.

The Navier-Stokes equations then give the following for the first two coordinates: $\frac{\partial p}{\partial r} = \frac{\partial p}{\partial \theta} = 0$, or $p = p(z)$. Then, according to the z coordinate:

$$\frac{1}{r}\frac{\partial v}{\partial r} + \frac{\partial v}{\partial\ \texttt{(equation(block: false, body: [r]), 2)}} = \frac{1}{\mu}\frac{\partial p}{\partial z} \tag{9}$$

Since the pressure does not depend on the variable r, this is an ordinary differential equation on $\frac{\partial v}{\partial r}$ whose general solution is:

$$v(r) = A\ln(r) + \frac{r^2}{4\mu}\frac{\partial p}{\partial z} + B \tag{10}$$

with $A = 0$ because the solution must not diverge at $r = 0$. Using the no-slip condition on the wall $v(R) = 0$, we obtain the known solution of Hagen-Poiseuille flow:

$$\boxed{v(r) = -\frac{R^2}{4\mu}\frac{\partial p}{\partial z}\left(1 - \frac{r^2}{R^2}\right)} \tag{11}$$

The volume flow rate is then:

$$\begin{aligned} Q &= \int_0^R \int_0^{2\pi} v(r) r dr d\theta \\ &= -\pi \frac{R^4}{8\mu} \frac{\partial p}{\partial z} \\ &= \pi R^2 \dot{z} \end{aligned} \tag{12}$$

because the fluid column advances in unison with the meniscus identified by the coordinate z. The pressure difference between the rear $z = 0$ and the front z due to viscosity is then:

$$\Delta p_\nu = -8 \frac{\mu}{R^2} z \dot{z} \tag{13}$$

Then, the hydrostatic pressure difference is expressed by $\Delta p_g = -\rho g z$ in the case of a vertical column, the term being negligible in a horizontal column. Finally, the Laplace pressure given by (2) is $\Delta p_L = \frac{2\sigma}{r} \cos\theta$. The total pressure difference in the pipe is therefore:

$$P_{\text{out}} - P_{\text{in}} = \Delta p_L + \Delta p_{\nu,l} + \Delta p_{\nu,g} + \Delta p_g \tag{14}$$

where $\Delta p_{\nu,l}$ is the differential in the fluid column between 0 and z, and $\Delta p_{\nu,g}$ is the differential in the gas column between z and L, which gives the expanded form of the pressure balance equation (6) with $\gamma = \frac{2\sigma}{r}$, $\cos\theta_c = \cos\theta$ and $\kappa = \frac{8}{r^2}$ as described by Garcia Eijo *et al.* [6].

II.3 Application of the Vaschy-Buckingham theorem to the problem of thermocapillarity

For the capillary filling problem with temperature gradient, we have the following quantities:

- The position of the meniscus z that we wish to model
- The variation in surface tension with temperature $\partial_T \sigma$, which we assume to be constant
- The temperature gradient ΔT applied in the channel of length L, height h and width w
- The physical properties of the fluid: dynamic viscosity μ, density ρ, thermal diffusivity α

We therefore have 9 variables available, allowing us to construct 5 dimensionless parameters using 4 variables. We choose μ, α, L and ΔT because we want to study the temperature gradient along the length. This results in the dimensionless parameters mentioned in this report. We can then construct the following model for the rate of fluid flow in the channel:

$$\frac{z}{L} = \mathcal{F}\left(\text{Ma}, \text{Pr}, \frac{w}{L}, \frac{h}{L}\right) \tag{15}$$

II.4 Reflections on modifying MKT theory in the presence of gradients

In Blake's original theory [26], the velocity of fluid advancing by capillary action is given by:

$$v = 2K\lambda \sinh\left(\frac{W}{\Delta nkT}\right) \tag{16}$$

where W is the work done per unit displacement along the three-phase contact line (liquid-gas-solid). This work is expressed for the Laplace force by

$$W = \sigma(\cos\theta_d - \cos\theta_s) \tag{17}$$

The objective would then be to add an additional term to this work, taking into account the variation in surface tension. However, two problems arise:

- We cannot directly inject $\partial_z \sigma$ as we were able to do in the pressure balance equation (6), because its unit is $\mathrm{N/m^2}$, which is incompatible with work per unit length.
- The Marangoni force is exerted tangentially to the surface of the fluid, and not along its line of contact. The movement of the latter is in fact a consequence of the rolling of the fluid, as discussed in Figure 26.

However, we know that the Marangoni force is a surface force, so on an infinitesimal surface element 'd'A, the elementary work required by this force to cause an elementary displacement δl would be:

$$\delta W = \nabla\sigma.\delta l.\ \mathrm{d}A \tag{18}$$

By placing ourselves along the line of contact and taking a rudimentary square approximation of the elementary surface $\mathrm{d}A$, we can assume that it is formed by the sides $\mathrm{d}c$, along the line of contact and therefore normal, and $\mathrm{d}x$, tangential. The gradient is expressed according to the latter direction, resulting in work per unit displacement δl:

$$\delta W = \nabla\sigma.\ \mathrm{d}\ A \approx \frac{\mathrm{d}\sigma}{\mathrm{d}x}\ \mathrm{d}x\ \mathrm{d}c = \mathrm{d}\ \sigma \tag{19}$$

This expression has the correct unit (N/m), but it is only a basic calculation that would need to be integrated along the contact line, which is not possible in general cases—or at least, not without knowing the exact expression. Furthermore, the term d σ remains difficult to interpret, since it is only a mathematical formalism that cannot be linked to physics (a local variation according to no variable).

With the aim of establishing a complete model of fluid flow in a rectangular microchannel in the presence of temperature gradients, the reader may wish to refer to the calculations by Goy *et al.* carried out in a circular channel [27].

II.5 Dimensionless numbers

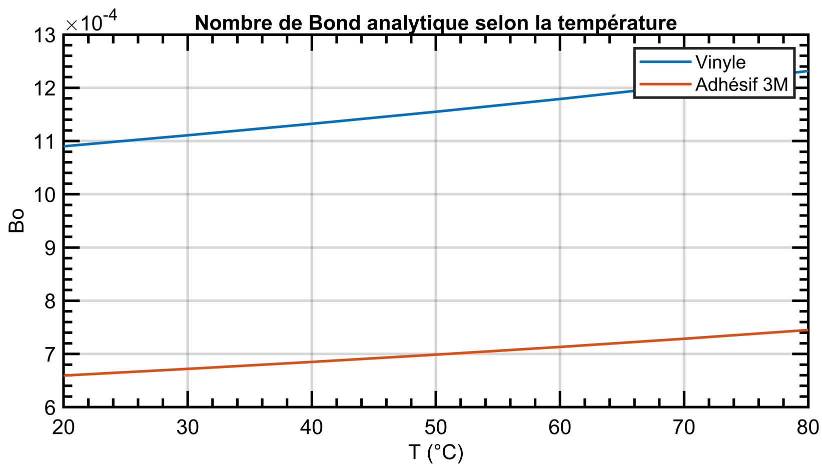

Figure 35: Bond number Bo calculated for various temperatures, for the straight channel with vinyl ($h = 90\ \mu$ m) and 3M adhesive ($h = 70\ \mu$ m).

III Numerical simulations

III.1 Pressure model

III.1.1 Inertial, viscous and capillary forces

In order to provide greater insight, viscous, capillary and inertial forces were evaluated based on the fundamental principle of dynamics according to the method of Azese *et al.*, with $f_v = f_\sigma + f_\mu$ [16]. The corresponding results are detailed Figure 36. The ratios f_v/f_σ and f_μ/f_σ tend towards 0 and -1, respectively, as in the study by Azese *et al.*, thus confirming the dominance of viscous effects over capillary effects. However, our results do not reproduce the trend $f_v/f_\sigma \approx 1$ at short times. This can be explained, on the one hand, by the accuracy of the analytical terms used by Azese *et al.*, and by the strong temperature dependence of the dimensionless terms in our experiments, a parameter that is not studied by Azese *et al.* Nevertheless, these results confirm the conclusions obtained from the analysis of the pressure terms Figure 11.

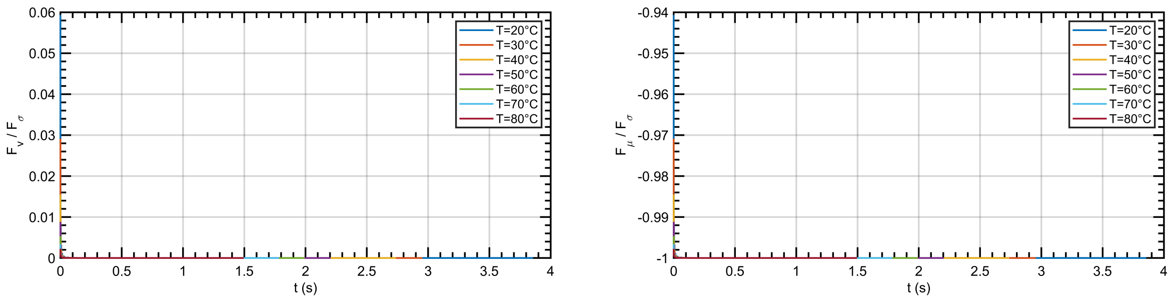

(a) Inertial force relative to capillary force f_v/f_σ

(b) Viscous forces relative to capillary force f_μ/f_σ

Figure 36: Comparison of the different forces at play in the fluid flowing through the capillary channel

III.1.2 J asymmetry metric

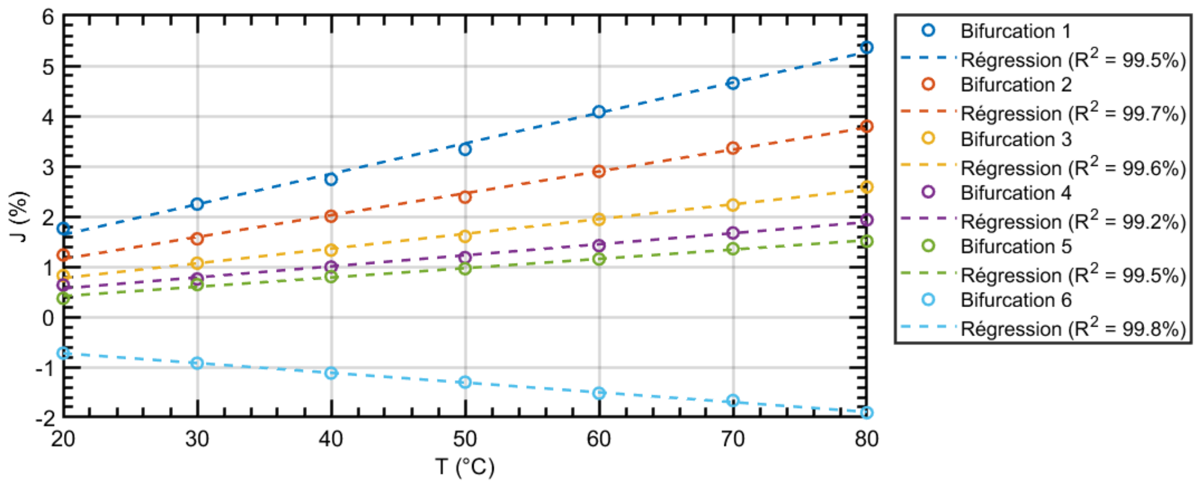

Figure 37: Asymmetry metric J calculated from the results of numerical integration for the comb chip for its bifurcations, as a function of temperature

III.2 Computer-aided design (CAD) model

The digital twin of the chip with Peltier cells is presented Figure 38. A so-called stationary thermal analysis is performed, with initial conditions of ambient temperature throughout the system and boundary conditions of convection with still air and imposed temperatures in the Peltier cells. Table 1 presents the material data used for the simulation. For glass, the density was calculated by measuring the weight and size of 50 laboratory slips. For vinyl, the density was calculated based on the specifications for Avery MPI 3800, and the thermal conductivity is a low value for PVC, a material that could have been used for this heat transfer vinyl. The thermal convection coefficient for exchange with air at rest is set at 5 $\mathrm{W.m^{-2}.K^{-1}}$, an average value given in the numerical modelling of structures course `MEC_4MS06_TA`.

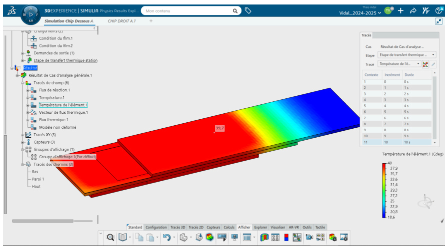

Figure 38: Screenshot of the 3DExperience software used to model temperature behaviour in the chip

Material	Glass	Vinyl
Density (kg/m^3)	2398.8	1780
Thermal conductivity ($W.m^{-1}.K^{-1}$)	1	0.1

Table 1: Material data used for simulation in 3DExperience computer-aided design software

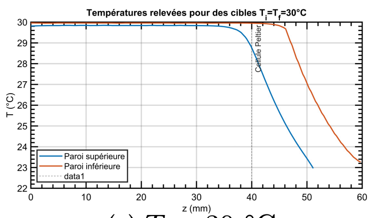

(a) $T = 30$ °C

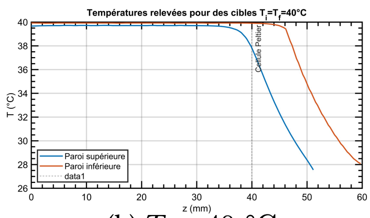

(b) $T = 40$ °C

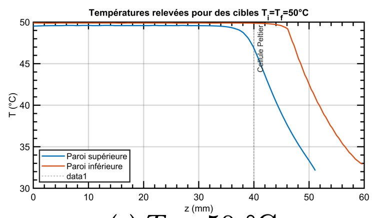

(c) $T = 50$ °C

Figure 39: Temperature readings on the lower and upper walls of the straight channel Figure 21 under uniform heating, modelled in 3DExperience and solved in steady-state thermal conditions.

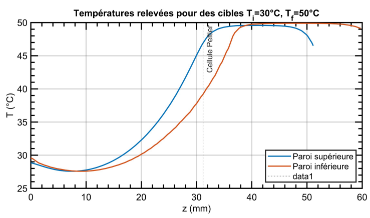

(a) $T_i = 30$ °C, $T_f = 50$ °C

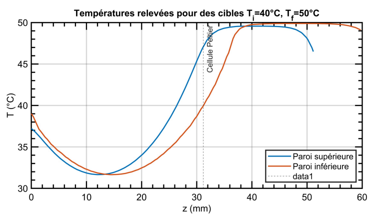

(b) $T_i = 40$ °C, $T_f = 50$ °C

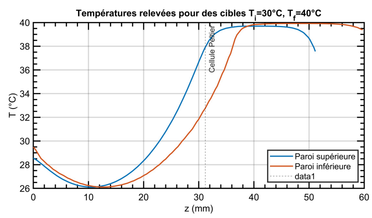

(c) $T_i = 30$ °C, $T_f = 50$ °C

Figure 40: Temperature readings on the lower and upper walls of the straight channel Figure 27 in the presence of temperature gradients, modelled in 3DExperience and solved in steady-state thermal conditions.

Heating both the upper and lower surfaces of the chip simultaneously would require increasing the number of Peltier cells, which would obstruct the observation area and make it impossible to view the experiments. Furthermore, the creation of a thermal gradient presents a problem of hollows that cannot be solved with Peltier devices, as these generate temperature plateaus (Figure 41). The gradients obtained are imperfect and very sensitive to slight cell displacement, greatly compressing the spatial gradient. Given the experimental durations (Figure 31), which are less than 3 s in most cases, the effect would not be observable. Further reducing the length of the channel is not feasible, as there is not enough time to reach the Lucas–Washburn asymptotic regime.

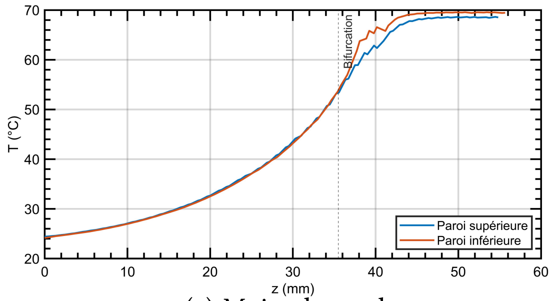

(a) Main channel

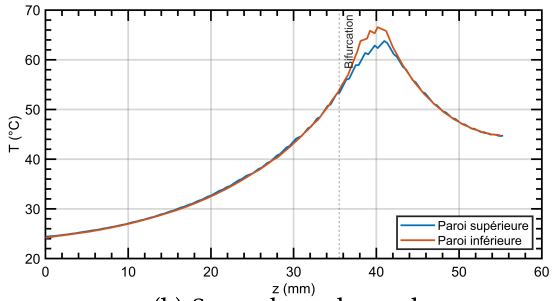

(b) Secondary channel

Figure 41: Temperature readings on the lower and upper walls of the T-shaped channel in air at ambient temperature 20 °C, with the main branch heated to $T = 70$ °C.

III.3 Surface resolution with Surface Evolver

In order to simulate the shape of the meniscus in the channel, I used Surface Evolver software. I based my work on the example of capillary rise in a circular tube (`capillary2.fe`, available at this link), and broke down the force, which was then defined in the same way across the entire wall, into four different contributions on the four straight edges, in order to take into account several contact angles. Finally, I empirically adjusted the force expressions to obtain a meniscus shape consistent with the work of Garcia Eijo *et al.* [8], in particular to form the correct contact angles on the correct walls.

I defined the capillary actions on the top/bottom and side walls of the rectangular microchannel as:

$$T_h = -\sigma \frac{\cos \theta_h}{h}, \; T_w = -\sigma \frac{\cos \theta_w}{w} \tag{20}$$

where $\cos \theta_h, \cos \theta_w$ are the contact angles formed by the fluid with the glass and vinyl, respectively. The forces integrated along the contact line of the top/bottom and side walls are then defined by:

$$\vec{F}_{w.h} = (-yzT_{w.h} xzT_{w.h} 0) \tag{21}$$

This is used to calculate an integral over a surface (according to Green's theorem), in this case the virtual rectangular surface corresponding to the rear of the fluid column.

After experimenting with the software and its commands, I have drawn several conclusions regarding its practical use:

- Not only must the mesh be refined regularly (command `r`), as shown in the examples in the documentation, but additional processing must also be applied: vertex averaging (command `V`), equitriangulation (command `u`)
- It is important that the domain is centred at (x, y, z) to ensure that the integrals are correctly defined, as these calculate circulation along a closed contour
- The capillary rise test, and therefore the integration of gravity, are necessary for calculating the static contact angle. The software does not define pressure concepts, so passive capillary filling is impossible
- Do not forget to add constraints so that the mesh remains within the domain at all times: via inequalities on the coordinates, but also by constraining the vertices of the edges to slide only vertically along the wall. Otherwise, energy minimisation may cause these edges and vertices to intersect, making the geometric shape physically impossible.

IV General methodology

IV.1 Experimental setup

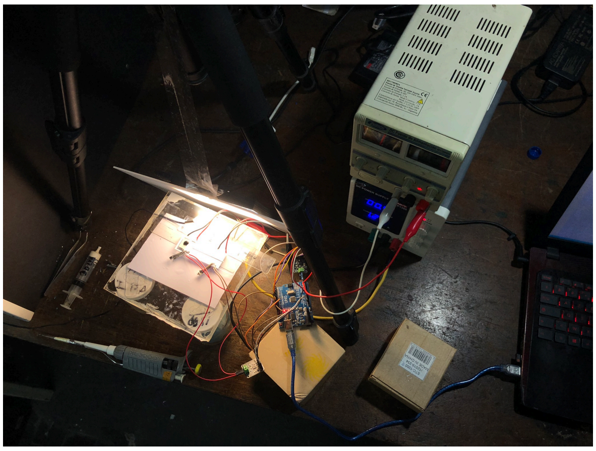

Figure 42: Photograph of the experimental setup for the temperature study.

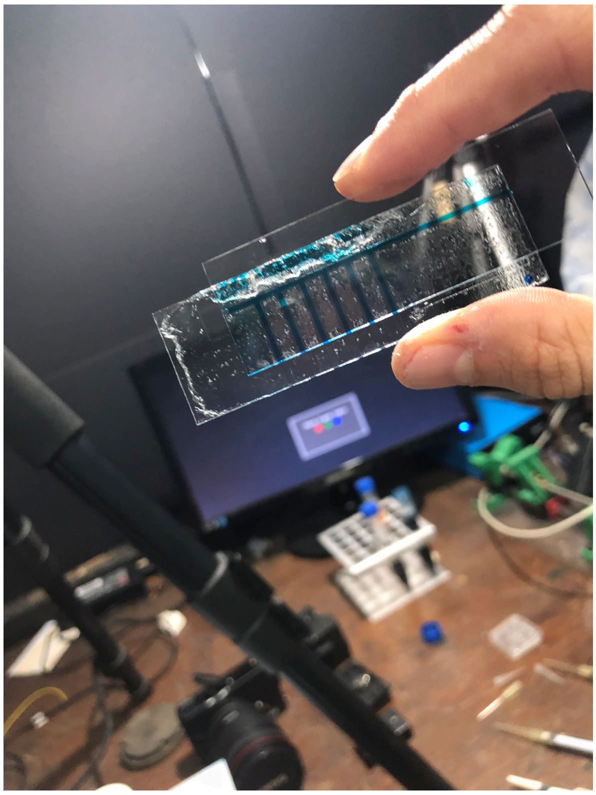

Figure 43: Photograph of an experimental comb-type chip made with 3M adhesive.

Figure 44: Photograph of the attempt to measure the contact angle by thermalisation. The device was placed in a kitchen oven.

IV.2 Digital filtering tests of meniscus velocity

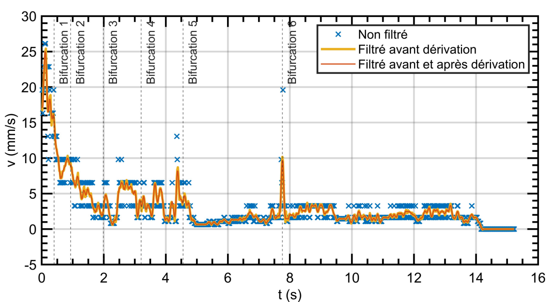

(a) Overview

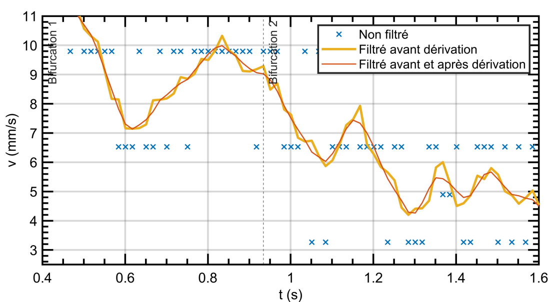

(b) Specification on a region

Figure 45: Meniscus velocity in path 6 of the comb chip as a function of time t at $T = 39.63$ °C: unfiltered ($\dot{z}$), filtered before derivation ($\partial_t \text{savgol}(z)$) and filtered before and after derivation. ($\text{savgol}(\partial_t \text{savgol}(z))$).

IV.3 Characterisation of voltage and current on the hot side of a Peltier cell

U (V)	I (A)	T (°C)
1	0,47	27,8
1,1	0,53	28,7
1,2	0,58	29,9
1,3	0,64	31,9
1,4	0,68	33
1,5	0,72	34,45
1,7	0,82	38,3
1,8	0,95	43,6
2	1,05	48,6
2,2	1,14	55
2,4	1,22	59,2
2,6	1,3	64,5
2,8	1,38	70,2
3	1,44	74,8
3,2	1,51	81,5
3,4	1,6	88,9
3,6	1,66	95,7

Table 2: Temperature readings T on the heated side of a Peltier cell, as a function of the voltage U imposed by the generator. The current I is measured directly on the generator.

V Experimental results

V.1 Comb-shaped

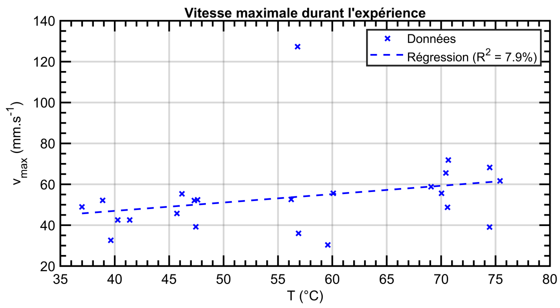

Figure 46: Maximum velocity reached by the meniscus during the experiment $v_{\max} = \max_t \dot{z}$ in path 6 of the comb chip, as a function of the measured temperature T. The linear regression is presented for illustrative purposes only.

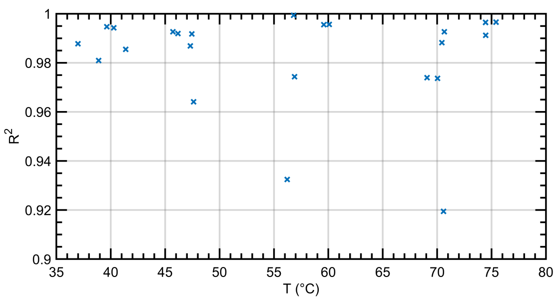

Figure 47: Coefficient of determination R^2 of the numerical optimisation of the DCAM regime (7) performed on experimental data from path 6 of the comb chip, as a function of the measured temperature T.

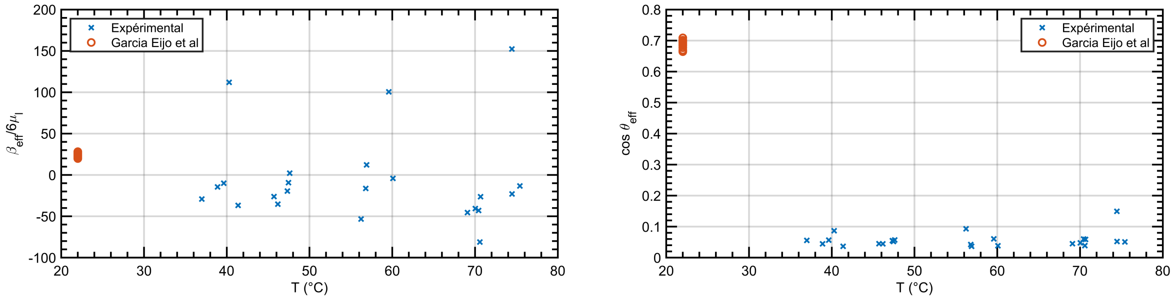

(a) Effective friction coefficient $\hat{\beta}_{\text{eff}} = \frac{\beta_{\text{eff}}}{6\mu}$ (b) Effective contact angle $\cos\theta_{\text{eff}}$

Figure 48: Optimised Dynamic Contact Angle Model (DCAM) parameters (7).

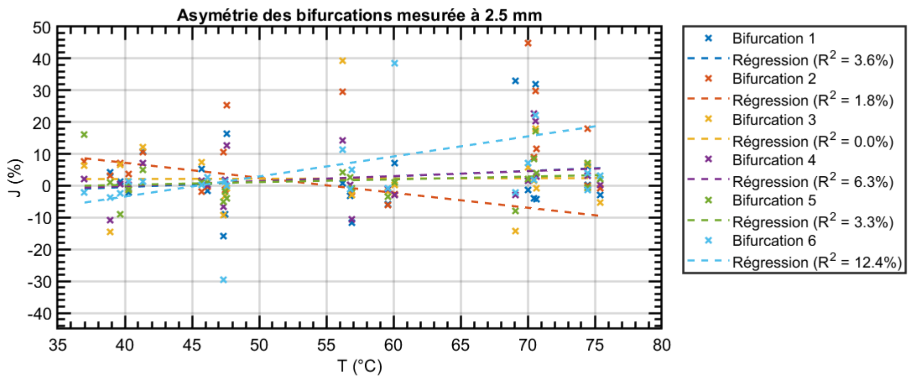

Figure 49: Asymmetry J with indicative linear regression; two outliers ($|J| > 100\%$) were excluded.

V.2 T-shaped

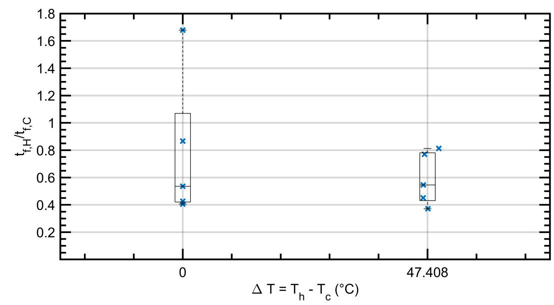

Figure 50: Ratio of filling times for the heated and unheated branches $\frac{t_{f,H}}{t_{f,C}}$ of the T-channel according to the temperature difference applied between these two branches $\Delta T = T_H - T_C$.

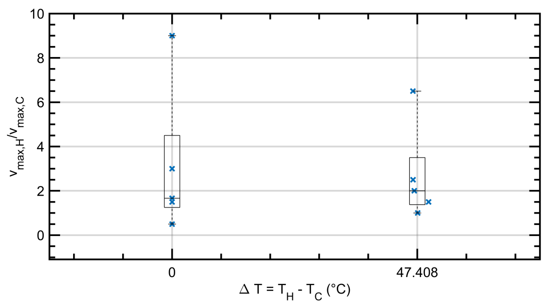

Figure 51: Ratio of maximum velocities reached in the heated and unheated branches $\frac{v_{\max,H}}{v_{\max,C}}$ of the T-channel according to the temperature difference applied between these two branches $\Delta T = T_H - T_C$.

V.3 Uniformly heated straight channel

V.3.1 Fluid dynamics

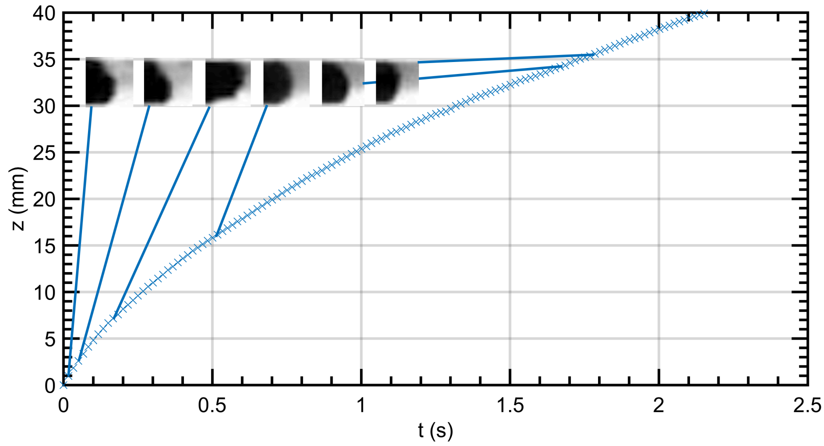

Figure 52: Evolution of the meniscus position with video captures for $T = 49.9$ °C.

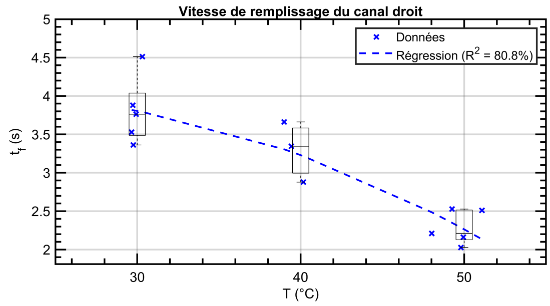

Figure 53: Filling time for the section of length $L = 40$ mm.

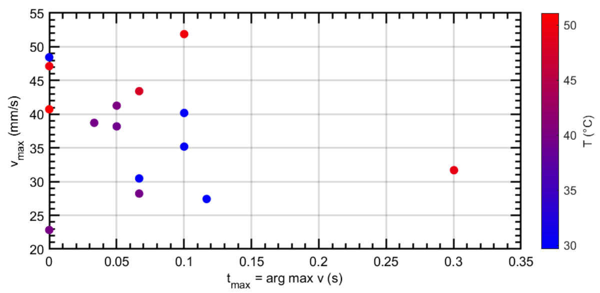

Figure 54: Maximum velocity depending on the time at which it is reached, coloured according to temperature.

V.3.2 Lucas-Washburn asymptotic regime and pressure terms

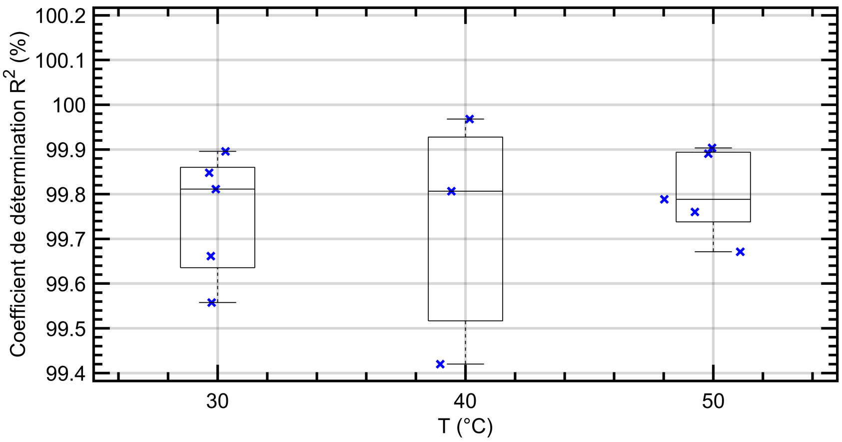

Figure 55: Values of the coefficient of determination R^2 for optimising the parameter $\sigma \cos\theta$.

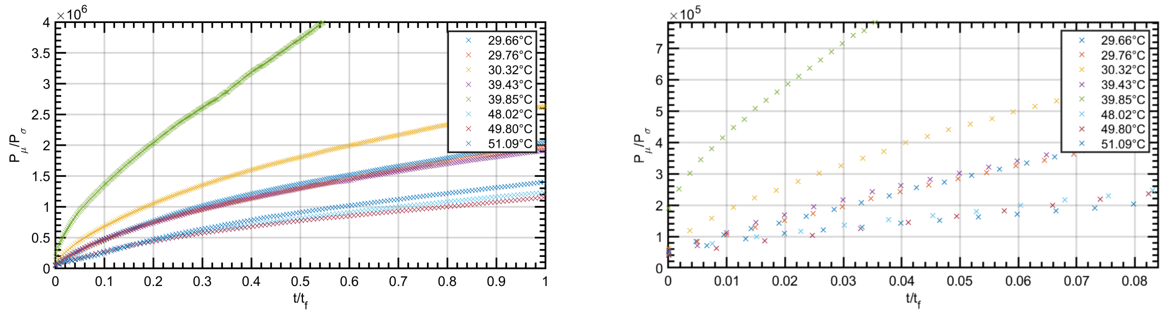

(a) Overview (b) Short-time behaviour specification

Figure 56: Evolution of the viscous and capillary pressure ratio, calculated with optimised $\sigma \cos \theta$.

V.4 Straight channel in the presence of gradients

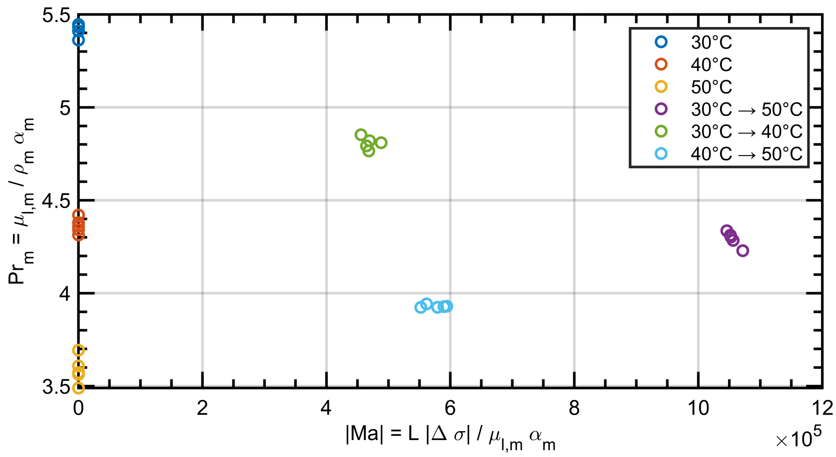

Figure 57: Marangoni number $|\mathrm{Ma}|$ and Prandtl number Pr calculated analytically from the measured temperatures during the experiments, under uniform loading (Section 3) and in the presence of gradients (Section 4).

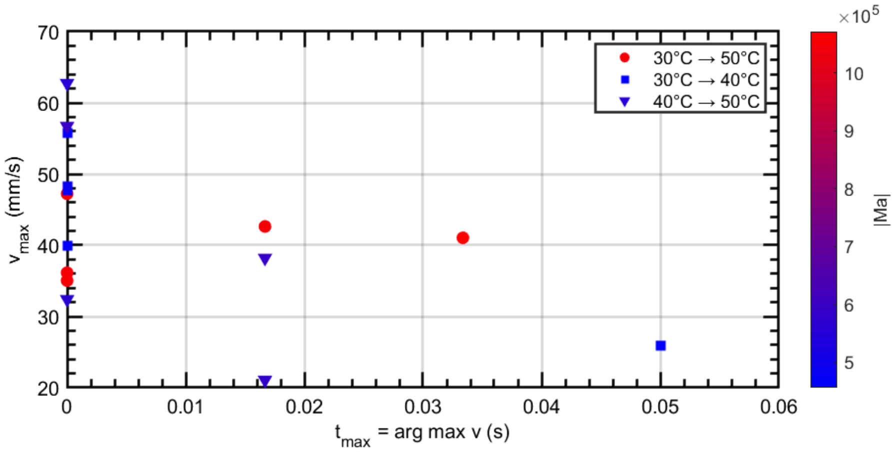

Figure 58: Maximum velocity $v_{\max} = \max_t \dot{z}(t)$ reached by the meniscus during the experiment, according to the time $t_{\max} = \arg\max_t \dot{z}$ at which it is reached. The colour scale represents the measured temperature T.

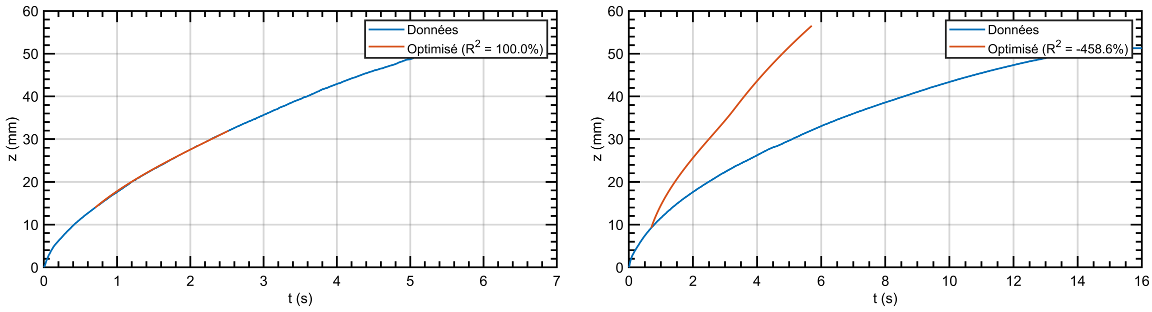

(a) $|\mathrm{Ma}| = 1.04 \times 10^6, \mathrm{Pr} = 5.43$

(b) $|\mathrm{Ma}| = 5.62 \times 10^5, \mathrm{Pr} = 3.49$

Figure 59: Examples of optimisation of the modified pressure balance equation in the presence of gradients (8).

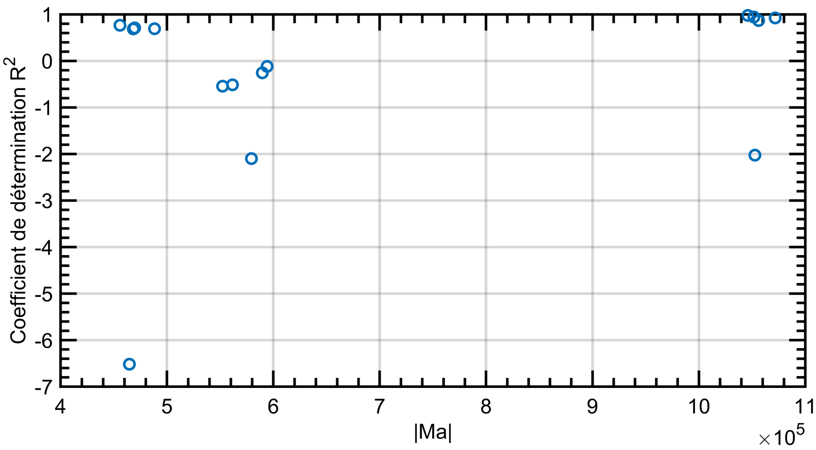

Figure 60: Coefficient of determination R^2 of the numerical optimisation of the term $\partial_z \sigma$ of the modified pressure balance equation performed on the experimental data, as a function of the Marangoni number $|\mathrm{Ma}|$.